- Full paper contribution
- XXX words in the main text, along with 8 tables and 15 figures

----

Numerical integration of an elasto-plastic critical state model for soils under unsaturated conditions

Author 1

- Martí Lloret-Cabot, Ph.D

Assistant Professor of Civil and Environmental Engineering
Department of Engineering
Durham University
UK

Author 2

- Simon J. Wheeler, Professor

Cormack Professor of Civil Engineering
James Watt School of Engineering
University of Glasgow
UK

Author 3

- Antonio Gens, Professor

Professor of Civil Engineering
Department of Civil and Environmental Engineering
Universitat Politècnica de Catalunya - CIMNE
Spain

Author 4

- Scott W. Sloan, Laureate Professor†

Professor of Civil Engineering
Priority Research Centre for Geotechnical Science and Engineering
The University of Newcastle
Australia.

†Laureate Professor Scott Sloan passed away unexpectedly during the preparation of this paper. The authors dedicate this work to his memory

ABSTRACT

This paper presents the complete set of incremental equations for the numerical integration of the Glasgow Coupled Model (GCM) and a comprehensive algorithm for its numerical integration. The incremental formulation proposed is expressed in terms of strain and suction increments (i.e. strain-driven) and defines an initial value problem (IVP) that can be solved once the initial state and the pair of increments of the driven variables are known. The numerical integration of this IVP is carried out by extending to unsaturated condition, the well-known explicit substepping formulation with automatic error control widely used for saturated soils. A notable feature of the substepping integration scheme presented is that it integrates simultaneously the model equations for both mechanical and water retention responses. Hence, the estimate of the local truncation error to automatically adjust the size of the integration step is not only affected by the local error in stresses and mechanical hardening parameter (as in a saturated soil model) but, additionally, by the local error incurred in the integration of the water retention relations (i.e. degree of saturation and water retention hardening parameter). The correctness of the integration scheme is then verified by comparison of computational outcomes against analytical/reference solutions.

1. INTRODUCTION

Advanced numerical methods have been applied to geomechanics during the last decades to solve geotechnical problems involving unsaturated soils (e.g. Pinyol et al., 2008, Borja and White, 2010, Cattaneo et al., 2014, Sheng et al., 2003ab, Gens, 2010, Khalili et al., 2008, Ng et al., 2000, Nuth and Laloui, 2008, Tsiampousi et al., 2013, Zhou and Sheng, 2015, Zhang et al., 2019). A key aspect in many of these numerical applications is the amount of water retained in the soil pores because it controls the loss or gain of soil's strength, critical to geotechnical instabilities. When the soil reaches full saturation after intense rainfall, for instance, all the additional contribution of the unsaturated condition to the soil strength vanishes. Changes in the saturation of the soil are also relevant to serviceability design because substantial volumetric compressions may occur during wetting (collapse) or drying (shrinkage) (Alonso et al., 1990, Gallipoli et al., 2003, Lloret-Cabot et al., 2014).

The amount of water stored within the pores of a soil is described by the water retention behaviour which relates the degree of saturation S_r (or the water content w) to matric suction s (where s is the difference between pore air pressure u_a and pore water pressure u_w). However, due to the occurrence of hysteresis, a one-to-one relation between S_r and s is rarely observed in soils (Romero et al., 1999, Tarantino 2009, Wheeler et al., 2003). In addition to this hysteresis, the water retention behaviour can be highly dependent on changes of the soil's porosity and, hence, on the mechanical behaviour (Romero et al., 1999, Tarantino 2009, Wheeler et al., 2003).

In order to represent accurately the potential changes in saturation when a soil is subjected to external environmental actions it is necessary to use a model that properly handles not only retention hysteresis but also the couplings between the mechanical behaviour and the water retention response. A model that includes all these effects is the Glasgow Coupled Model GCM (Wheeler et al., 2003; Lloret-Cabot et al., 2013), and the major focus of this paper is the development of an integration scheme capable to integrate, accurately and efficiently, the incremental constitutive relations of this model.

The explicit substepping formulation with automatic error control proposed in Sloan, (1987) and Sloan et al. (2001) has been extensively used in the literature for the numerical integration of elasto-plastic models for saturated soils (Sloan et al., 2001, Abbo, 1997, Sheng et al., 2000, Pedroso et al., 2008, Zhao et al., 2005, Pérez-Foguet et al., 2001). Full extension of this formulation to the unsaturated case is presented in this paper in the context of the GCM. The extended substepping integration scheme integrates simultaneously the model equations for both mechanical and water retention responses. Hence, the local error incurred during the numerical integration of the model is not only affected by the local error in stresses and mechanical hardening parameters (as in the saturated case) but, additionally, by the local error incurred in the integration of the water retention relations. A consequence of this is that the measure of the local error used in a substepping integration scheme to adjust automatically the size of the next integration step is now estimated accounting for both sources of numerical error, including the inexact integration of the mechanical and water retention relations. Equivalent conclusions are reached when integrating other coupled constitutive models for unsaturated soils with substepping integration schemes with automatic error control (Zhang and Zhou, 2016).

The paper presents a comprehensive algorithm for the numerical integration of the GCM. Although some aspects of the algorithm are linked to specific features of the GCM, the overall approach is general and can be applied to other coupled constitutive models for unsaturated soils.

A small reformulation of the GCM is first presented with the aim of simplifying its numerical integration. Based on this reformulation, the relevant incremental mechanical and water retention relations of the model for each possible response, including unsaturated and saturated conditions, are developed. Two explicit substepping integration schemes with automatic error control are proposed in order to investigate the accuracy of the numerical integration: the second order modified Euler with substepping and the fifth order Runge-Kutta-Dormand-Prince with substepping. A verification study is presented at the end of the paper extending to unsaturated conditions, the verification strategy proposed in Lloret-Cabot et al. (2016) for saturated soils.

2. REFORMULATING GCM

Certain aspects of the GCM are reformulated in this section with the aim of simplifying its numerical integration. This reformulation does not involve any modification of the model, simply a change in how it is presented.

The version of the GCM presented here is that given in Lloret-Cabot et al. (2017), which assumes that there are no elastic changes of degree of saturation (the gradient of elastic scanning curves in the water retention plane is zero i.e. $\kappa_s = 0$ in the original model of Wheeler et al., 2003), in order to achieve consistent behaviour across transitions between unsaturated and saturated states.

Soil mechanics sign convention is adopted hereafter (compression positive). Vectors and tensors are indicated in bold and the superscript T indicates transposed.

2.1. Mechanical Behaviour

The mechanical behaviour describes the stress-strain relations. In the GCM, strains are related to the "Bishop's stress" tensor $\boldsymbol{\sigma}^*$, defined as:

$$\boldsymbol{\sigma}^* = \boldsymbol{\sigma} - \mathbf{m}^T \left(S_r u_w - (1 - S_r) u_a \right) = \bar{\boldsymbol{\sigma}} + \mathbf{m}^T S_r s \qquad (1)$$

where $\boldsymbol{\sigma}$ is the total stress tensor, $\mathbf{m}^T = (1,1,1,0,0,0)$ an auxiliary vector, S_r the degree of saturation, u_a the pore air pressure, u_w the pore water pressure, s matric suction and $\bar{\boldsymbol{\sigma}}$ net stress tensor ($\bar{\boldsymbol{\sigma}} = \boldsymbol{\sigma} - \mathbf{m}^T u_a$). Equation 1 reverts to the saturated effective stress tensor $\boldsymbol{\sigma}'$ (i.e. $\boldsymbol{\sigma}' = \boldsymbol{\sigma} - \mathbf{m}^T u_w$) when $S_r = 1$.

2.1.1 Elastic response

The incremental elastic relationship between Bishop's stress and strains is given by:

$$\mathrm{d}\boldsymbol{\sigma}^* = \mathbf{D_e} \mathrm{d}\boldsymbol{\varepsilon} \qquad (2)$$

where d refers to an infinitesimal variation and $\mathbf{D_e}$ is the elastic stiffness matrix:

$$\mathbf{D_e} = \begin{pmatrix} K + \frac{4}{3}G & K - \frac{2}{3}G & K - \frac{2}{3}G & 0 & 0 & 0 \\ & K + \frac{4}{3}G & K - \frac{2}{3}G & 0 & 0 & 0 \\ & & K + \frac{4}{3}G & 0 & 0 & 0 \\ \textit{symmetric} & & & G & 0 & 0 \\ & & & & G & 0 \\ & & & & & G \end{pmatrix} \qquad (3)$$

K and G in Equation 3 are, respectively, the elastic tangential bulk and shear moduli defined as:

$$K = \frac{\mathrm{d}p^*}{\mathrm{d}\varepsilon_v^e} = \frac{vp^*}{\kappa} \quad (4)$$

$$G = \frac{\mathrm{d}q}{3\mathrm{d}\varepsilon_d^e} \quad (5)$$

where p^* is the mean Bishop's stress, q is the deviatoric stress, ε_v^e is the elastic volumetric strain, ε_d^e is the elastic deviatoric strain, v is the specific volume and κ is the gradient of a swelling line in the v:ln p^*plane. A variety of expressions are possible for G (Potts and Zdravkovic, 1999), but the simplest is to assume a constant value of shear modulus.

Given that $\boldsymbol{\sigma}^* = \boldsymbol{\sigma}'$ when $S_r = 1$, Equation 2 has the advantage of converging naturally to the conventional saturated elastic relations of the Modified Cam Clay model, MCC (Roscoe and Burland, 1968).

2.1.2. Mechanical yield curve

In order to reduce potential inaccuracies in the evaluation of the mechanical yield curve f_{M}, Sheng et al. (2000) propose that f_{M} is normalised against a stress parameter, so that its evaluation is not significantly influenced by the magnitude of stresses. Using the preconsolidation stress p^*_0 (also referred to as the mechanical yield stress) as a normalising factor, the general expression for the mechanical yield curve of the GCM is (Lloret-Cabot et al., 2013):

$$f_{\mathrm{M}} = \frac{3J_2}{\left(p_0^*\right)^2} + \mathrm{M}\left(\theta\right)^2\left[\left(\frac{p^*}{p_0^*}\right)^2 - \frac{p^*}{p_0^*}\right] = 0 \quad (6)$$

where J_2 is the second invariant of the deviatoric stress tensor $\mathbf{s}$ (i.e. $\mathbf{s} = \boldsymbol{\sigma}^* - \mathbf{m}^T p^*$) and M($\theta$) is a function of the Lode's angle θ describing the shape of the mechanical yield surface in the deviatoric plane (Potts and Gens, 1984). Available expressions for M(θ) in the literature for saturated conditions (e.g. Potts and Gens, 1984, Potts and Zdravkovic, 1999, Sheng et al., 2000) can be readily incorporated to the unsaturated case. However, for simplicity, M is assumed constant herein. Then, for axisymmetric conditions, the mechanical yield curve becomes:

$$f_{\mathrm{M}} = \frac{q^2}{\left(p_0^*\right)^2} + \mathrm{M}^2\left[\left(\frac{p^*}{p_0^*}\right)^2 - \frac{p^*}{p_0^*}\right] = 0 \quad (7)$$

where M is the slope of the critical state line in the q:p^* plane and q is the deviatoric stress i.e. $q^2 = 3J_2$.

Expressions for M(θ) are possible by extending to the unsaturated case available expressions in the literature for saturated conditions (e.g. Potts and Gens, 1984, Potts and Zdravkovic, 1999, Sheng et al., 2000). For simplicity, axisymmetric conditions are assumed in the formulation presented here, so that M can be assumed a soil constant.

The preconsolidation stress p^*_0 varies with the degree of saturation S_r according to:

$$p_0^* = p'_0 \exp\left(\frac{k_1}{\lambda_s}\left(1-S_r\right)\right) \tag{8}$$

where p'_0 is the value of the saturated preconsolidation stress. k_1 and λ_s are soil constants.

Equation 6 indicates that the mechanical yield curve f_M is elliptical in shape (of aspect ratio M) when plotted in the q:p^* plane (Figure 1). The size of this ellipse is defined by the current value of mechanical yield stress p^*_0, and this varies linearly with the degree of saturation in the S_r: lnp^* plane (Equation 8). For the special case of S_r = 1, the mechanical yield curve corresponds to the conventional ellipse of the MCC (Figure 1), because $p^*_0 = p'_0$, which simplifies the implementation of the GCM in finite element programs where the MCC is already available.

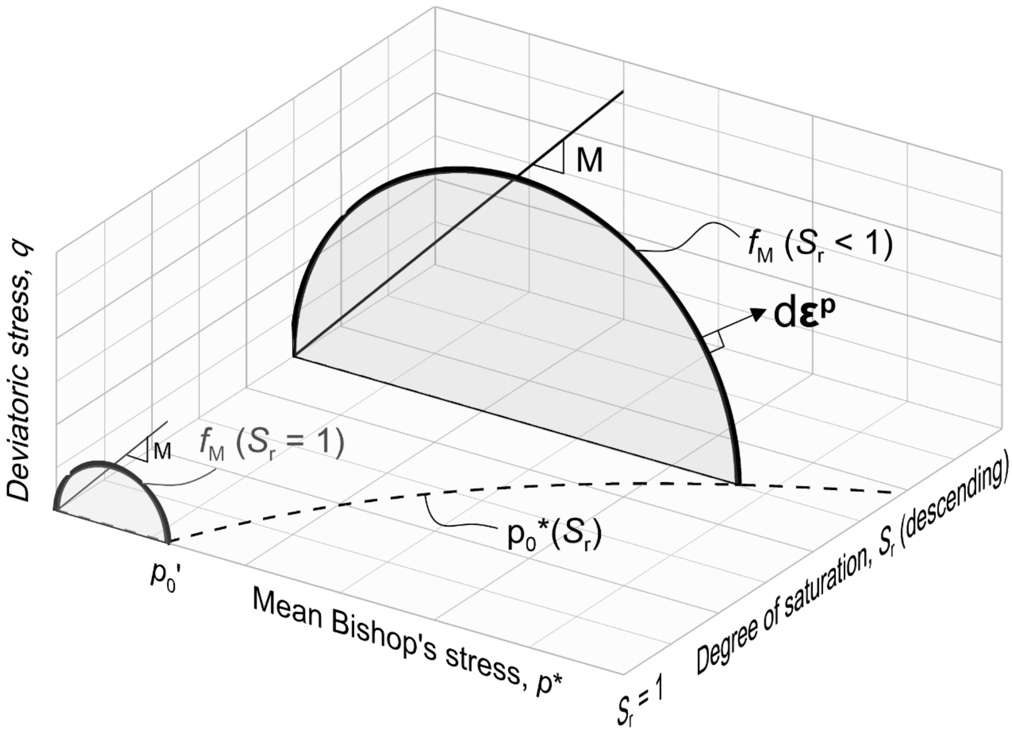

Figure 1 Typical mechanical yield curves of the GCM for a general value of S_r and for S_r =1 in the p^*:q:S_r space.

Interestingly, the new form of expressing the variations of mechanical yield stress with degree of saturation given by Equation 8 resembles the expression proposed by Jommi and Di Prisco (1994), with the difference here that the GCM represents the variation of degree of saturation within a single constitutive framework. Some of the advantages in constitutive modelling of expressing the mechanical (Bishop's) yield stress p^*_0 in terms of degree of saturation are discussed in Lloret-Cabot & Wheeler (2018). Also, when the mechanical yield condition in GCM is represented in terms of Bishop's stresses and degree of saturation (as in Figure 1), there is no movement of the yield surface until the soil state reaches the surface. This contrasts with the original presentation of the GCM in Wheeler et al. (2003), where coupled movements of the mechanical yield surface (expressed there in terms of Bishop's stresses and modified suction s^* (defined later)) occur during yielding on water retention yield surfaces. As a consequence, the new formulation has advantages in numerical modelling. Firstly, it is easier to use various common numerical techniques that have been developed to overcome issues arising when performing explicit numerical integration of saturated elasto-plastic critical state models (e.g. yield intersection, elasto-plastic unloading, drift correction, etc). Secondly, as demonstrated later, this specific form of f_M facilitates the formulation of an unambiguous strategy to identify the correct model response activated by any given stress path. Finally, it provides a very simple representation of the transitions between saturated and unsaturated conditions that avoids the drawbacks discussed in Pedroso et al. (2008) about the non-convex form of the mechanical yield curve at the transition from unsaturated to saturated states.

2.1.3. Hardening law

Given that the saturated preconsolidation stress p'_0 remains constant unless mechanical yielding occurs, it is possible to relate p'_0 to changes of plastic volumetric strains $\mathrm{d}\varepsilon_v^p$ through the following hardening law:

$$\frac{\mathrm{d}p'_0}{p'_0} = \frac{v}{\lambda - \kappa}\mathrm{d}\varepsilon_v^p \qquad (9)$$

where κ is the gradient of a swelling line (in the v:ln p' plane for saturated conditions and the v:ln p^* plane for unsaturated conditions) and λ is the gradient of the saturated normal compression line in the v:ln p' plane.

Equation 9 is valid whether the soil is under saturated or unsaturated conditions and, as in the Barcelona Basic Model of Alonso et al. (1990), p'_0 can be viewed in the GCM as the mechanical hardening parameter. Equation 9 is identical to the conventional volumetric hardening law of the MCC which, as highlighted earlier, is helpful when combining existing critical state finite element formulations for saturated soils with the GCM.

2.1.4. Flow rule

An associated flow rule is adopted for the mechanical behaviour:

$$\mathrm{d}\boldsymbol{\varepsilon}^{\mathbf{p}} = \mathrm{d}\lambda_{\mathrm{M}} \frac{\partial f_{\mathrm{M}}}{\partial \boldsymbol{\sigma}^{*}} \tag{10}$$

where $\mathrm{d}\lambda_{\mathrm{M}}$ is an unknown positive scalar (referred to as the mechanical plastic multiplier) to be found by imposing that the stress point remains on f_{M} during mechanical yielding (consistency condition).

2.1.5. Analytical relations for the mechanical behaviour

The relationships for the mechanical behaviour of the GCM just presented lead to the following analytical expressions for isotropic normal compression states and critical states. These analytical expressions are relevant for verification purposes and provide further insight on specific features of the GCM. For example, isotropic stress states involving yielding on f_{M} are predicted to lie on a normal compression line in the v:lnp^* plane, the position of which depends on the current value of S_r (see also Lloret-Cabot et al. 2018ab):

$$v = \mathrm{N}\left(S_r\right) - \lambda \ln p^{*} \tag{11}$$

where

$$\mathrm{N}\left(S_r\right) = \mathrm{N} + \frac{k_1\left(\lambda - \kappa\right)\left(1 - S_r\right)}{\lambda_s} \tag{12}$$

and N is the intercept of the conventional saturated normal compression line (see Figure 2).

Critical states, on the other hand, are defined by:

$$q = \mathrm{M}p^{*} \tag{13}$$

$$v = \Gamma\left(S_r\right) - \lambda \ln p^{*} \tag{14}$$

where q is the deviatoric stress and

$$\Gamma(S_r) = \mathrm{N}(S_r) - (\lambda - \kappa)\ln 2 = \Gamma + \frac{k_1(\lambda - \kappa)(1 - S_r)}{\lambda_s} \tag{15}$$

and Γ is the intercept of the conventional saturated critical state line (see Figure 2).

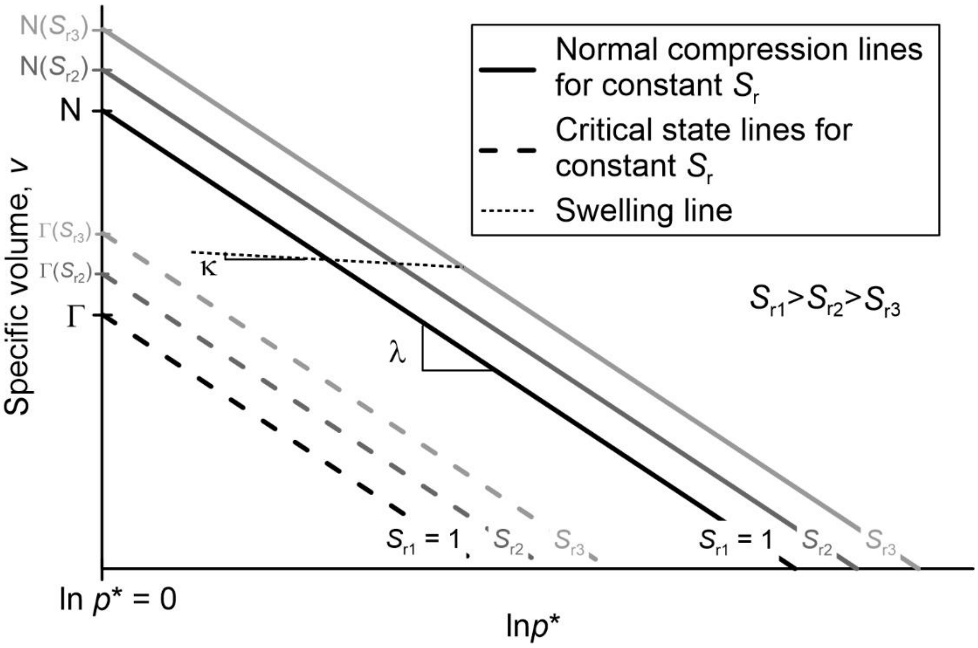

Figure 2. Normal compression and critical state lines for constant values of S_r in the v:lnp^* plane.

2.2. Water Retention Behaviour

Water retention behaviour is typically expressed in terms of degree of saturation S_r and matric suction s, however, based on the work of Houlsby (1997), the GCM relates S_r to the "modified suction" s^*, defined as:

$$s^* = n(u_a - u_w) = \frac{v-1}{v}s \tag{16}$$

where n is porosity.

2.2.1. Elastic response

For situations where the GCM is to be used for both unsaturated and saturated conditions, Lloret-Cabot et al. (2017) recommends to assume that elastic variations of degree of saturation are zero $\mathrm{d}S_r^e = 0$ (the gradient in the original model of Wheeler et al. (2003) of elastic scanning curves in the S_r:lns^* plane is zero i.e. $\kappa_s = 0$). The same assumption is made here.

2.2.2. Retention yield curves

Water retention behaviour is described by two yield functions: the wetting retention yield curve f_{WR} and the drying retention yield curve f_{DR}. Variations of modified suction occurring inside f_{WR} and f_{DR} result in no changes of S_r (i.e. dS_r = $dS_r^e = 0$). Yielding on f_{WR} produces plastic increases of S_r (i.e. dS_r = $dS_r^p > 0$), whereas yielding on f_{DR} causes plastic decreases of S_r (i.e. dS_r = $dS_r^p < 0$). Similarly to the mechanical yield curve, the expression of the wetting retention yield curve is also normalised:

$$f_{WR} = \frac{s_1^* - s^*}{s_1^*} = 0 \qquad (17)$$

where s_1^* is the wetting yield stress controlling the occurrence of yielding on f_{WR} (equivalent to p_0^* for mechanical yielding).

The wetting yield stress s_1^* varies with the occurrence of mechanical yielding according to:

$$s_1^* = s_{10}^* \left(\frac{p'_0}{p'_{00}} \right)^{k_2} = s_{10}^* \exp\left(\frac{-k_2}{\lambda - \kappa} \Delta v^p \right) \qquad (18)$$

where k_2 is a coupling parameter, p'_0 is the mechanical hardening parameter and Δv^p indicates plastic decreases of specific volume from a reference state. s_{10}^* and p'_{00} are, respectively, the values of s_1^* and p'_0 at the reference states when $\Delta v^p = 0$.

Similarly, the expression of the drying retention yield curve is:

$$f_{DR} = \frac{s^* - s_2^*}{s_2^*} = 0 \qquad (19)$$

where s_2^* is the drying yield stress for f_{DR} which varies with p'_0 (or Δv^p) according to:

$$s_2^* = s_{20}^* \left(\frac{p'_0}{p'_{00}} \right)^{k_2} = s_{20}^* \exp\left(\frac{-k_2}{\lambda - \kappa} \Delta v^p \right) \qquad (20)$$

where s_{20}^* and p'_{00} are, respectively, the values of s_2^* and p'_0 when $\Delta v^p = 0$.

Equations 17 and 19 indicate, respectively, that the wetting retention yield curves f_{WR} and the drying retention yield curve f_{DR} form two parallel straight lines when plotted in the lns^*:lnp_0' plane (see Figure 3). The positions of these straight lines and their gradient with respect to lnp_0' are given by Equations 18 and 20. The current values of the parameters s_{10}^* and s_{20}^* (which correspond, respectively, to the values of s_1^* and s_2^* at a reference state in which $p'_0 = p'_{00}$) fix the position of f_{WR} and f_{DR} respectively, whereas the gradient is given by the value of the soil parameter k_2. Therefore, the parameters s_{10}^* and s_{20}^* are equivalent to the mechanical hardening parameter p_0' and, hence, can be viewed as the hardening parameters of the water retention response. Equations 17-20 are still active under fully saturated conditions, because they track the influence of mechanical yielding on the potential occurrence of desaturation on drying (i.e. air-entry point) and re-saturation on wetting or loading (i.e. air-exclusion point).

The spacing between f_{WR} and f_{DR} is assumed constant when plotted in terms of $\ln s^*$ (i.e. $s_2^* = R \cdot s_1^*$, where R is a soil constant (Lloret-Cabot et al., 2017) and this spacing defines the current range of values of s^* for which no plastic changes of S_r will occur at a given value of p'_0. Hence, the spacing between f_{WR} and f_{DR} in the $\ln s^*$:$\ln p_0'$ plane defines the elastic domain of the water retention behaviour (see shaded zone in Figure 3). Yielding on the drying retention yield curve reduces the values of S_r and causes a coupled movement of the wetting retention yield curve (Wheeler et al., 2003). Equivalent comments apply when yielding on f_{WR}.

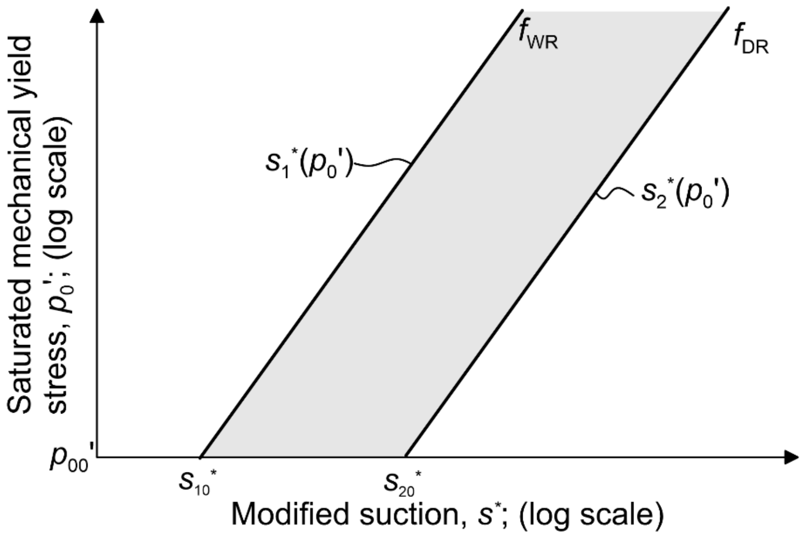

Figure 3. Water retention yield curves in $\ln s^*$:$\ln p_0'$ plane.

2.2.3. Hardening law

Given that s_{10}^* and s_{20}^* remain constant unless water retention yielding occurs, it is possible to relate them to plastic changes of degree of saturation $\mathrm{d}S_r^p$ through the following hardening law:

$$\frac{\mathrm{d}s_{10}^*}{s_{10}^*} = \frac{\mathrm{d}s_{20}^*}{s_{20}^*} = \frac{-\mathrm{d}S_r^p}{\lambda_s} \qquad (21)$$

where λ_s is the gradient of a main wetting/drying curve in the S_r:lns^* plane.

For completeness, it is useful to include here how the water retention yield stress s_R^* (where the subscript R is 1 for f_{WR} and 2 for f_{DR}) vary against the water retention and mechanical hardening parameters:

$$\frac{\mathrm{d}s_R^*}{s_R^*} = \frac{\mathrm{d}s_{R0}^*}{s_{R0}^*} + k_2 \frac{\mathrm{d}p'_0}{p'_0} \qquad (22)$$

Similarly, the mechanical yield stress p_0^* varies with the mechanical and water retention hardening parameters according to:

$$\frac{\mathrm{d}p_0^*}{p_0^*} = \frac{\mathrm{d}p'_0}{p'_0} + k_1 \frac{\mathrm{d}s_{R0}^*}{s_{R0}^*} \qquad (23)$$

2.2.4. Flow rule

Associated flow rules are assumed for the water retention response:

$$\mathrm{d}S_r^p = \mathrm{d}S_r = -\mathrm{d}\lambda_R \frac{\partial f_R}{\partial s^*} \qquad (24)$$

where $\mathrm{d}\lambda_R$ is an unknown positive scalar (referred to as the water retention plastic multiplier) to be found by imposing that the stress point remains on f_R during retention yielding (consistency condition).

Given that $\mathrm{d}S_r^e = 0$ (Figure 4), total and plastic variations of S_r are the same ($\mathrm{d}S_r = \mathrm{d}S_r^p$).

2.2.5. Analytical relations for the water retention behaviour

The water retention relations just presented result in the following expressions for main wetting and drying curves:

$$S_r = 1 - \lambda_s \ln\left(\frac{s^*}{s_{ex}^*}\right) \qquad (25)$$

$$S_r = 1 - \lambda_s \ln\left(\frac{s^*}{s_e^*}\right) \qquad (26)$$

where s_{ex}^* and s_e^* are, respectively, the current air-exclusion and air-entry values of modified suction (see Figure 4). These air-exclusion and air-entry values of modified suction are related to the saturated preconsolidation stress p_0' through the saturation and desaturation lines, respectively (Lloret-Cabot et al., 2017):

$$\ln s_{ex}^* = \frac{\left(\Omega^* - 1\right)}{\lambda_s^*} + k_2 \ln p'_0 \tag{27}$$

$$\ln s_e^* = \frac{\left(\Omega^* - 1\right)}{\lambda_s^*} + k_2 \ln p'_0 + \ln R \tag{28}$$

where λ_s^* and Ω^* are soil constants corresponding to the gradient and intercept, respectively, of the unsaturated normal compression planar surface for S_r derived in Lloret-Cabot et al. (2017). λ_s^* can be expressed in terms of soil constants λ_s, k_1 and k_2 and Ω^* can be expressed in terms of soil constants N, N^*, λ, κ, λ_s and k_1 (see Appendix A), where N^* is the intercept of the unsaturated normal compression planar surface for v derived in Lloret-Cabot et al. (2017).

Combining main wetting and main drying equations with the saturation and desaturation lines, respectively, the expressions of the main wetting and main drying curves can be expressed in terms of p'_0:

$$S_r = 1 + \left[\left(\Omega^* - 1\right)\left(1 - k_1 k_2\right) + k_2 \lambda_s \ln p'_0\right] - \lambda_s \ln s^* \tag{29}$$

$$S_r = 1 + \left[\lambda_s \ln R + \left(\Omega^* - 1\right)\left(1 - k_1 k_2\right) + k_2 \lambda_s \ln p'_0\right] - \lambda_s \ln s^* \tag{30}$$

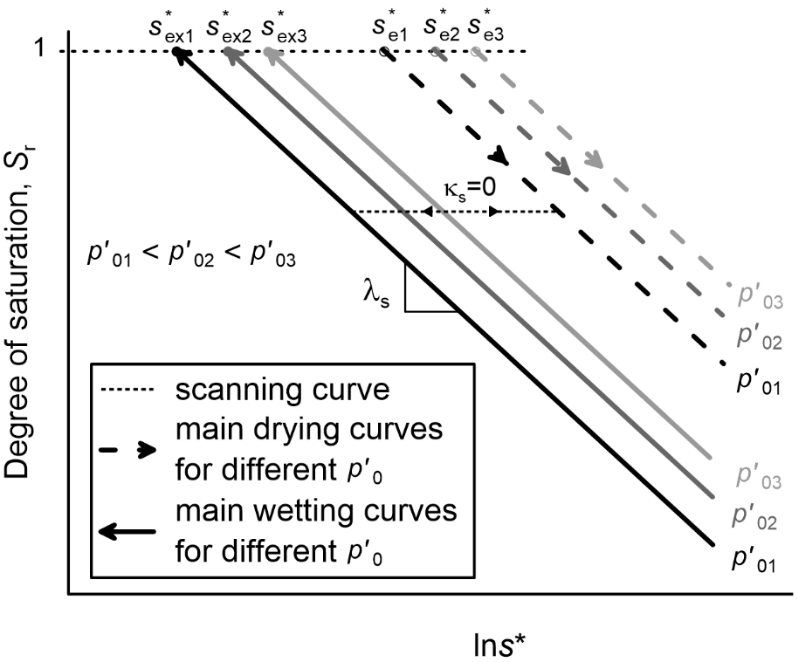

Figure 4. Main wetting and main drying water retention curves for constant values of p_0' in the S_r:lns^* plane.

2.3. Model responses

There are six possible responses in the GCM to represent mechanical and water retention behaviour of soils under saturated and unsaturated conditions. Each of them is identified hereafter by an integer number assigned to the variable “STRPTH”:

(1) STRPTH=1 is for purely elastic behaviour ($\Delta\boldsymbol{\varepsilon}^{\mathbf{p}} = \mathbf{0}$ and $\Delta S_r = 0$).
(2) STRPTH=2 is for yielding on only f_{WR} ($\Delta\boldsymbol{\varepsilon}^{\mathbf{p}} = \mathbf{0}$ and $\Delta S_r > 0$).
(3) STRPTH=3 is for yielding on only f_{DR} ($\Delta\boldsymbol{\varepsilon}^{\mathbf{p}} = \mathbf{0}$ and $\Delta S_r < 0$).
(4) STRPTH=4 is for yielding on only f_{M} ($\Delta\boldsymbol{\varepsilon}^{\mathbf{p}} \neq \mathbf{0}$ and $\Delta S_r = 0$).
(5) STRPTH=5 is for simultaneous yielding on f_{M} and f_{WR} ($\Delta\boldsymbol{\varepsilon}^{\mathbf{p}} \neq \mathbf{0}$ and $\Delta S_r > 0$).
(6) STRPTH=6 for simultaneous yielding on f_{M} and f_{DR} ($\Delta\boldsymbol{\varepsilon}^{\mathbf{p}} \neq \mathbf{0}$ and $\Delta S_r < 0$).

Transitions from unsaturated to saturated conditions (saturation) occur whilst on f_{WR}. This means that an initially unsaturated soil ($S_r < 1$) can only saturate during stress paths that involve yielding on f_{WR} (i.e. STRPTH=2 or STRPTH=5). Once the soil is saturated, further increases of S_r are prevented (i.e. flow rule no longer applies on f_{WR}) and the consistency condition on f_{WR} is removed so that the stress point can pass beyond f_{WR} (see Lloret-Cabot et al., 2017, Lloret-Cabot et al., 2018ab for details).Transitions in the reverse direction (desaturation), occur whilst on f_{DR}. In this case, an initially saturated soil ($S_r = 1$) can only desaturate during stress paths that involve yielding on f_{DR} (i.e. STRPTH=3 or STRPTH=6).

Typical examples of the six possible responses in the GCM are illustrated in Figure 5 for unsaturated states. Each response is represented by a pair of plots. The top plot shows the water retention behaviour in the $\ln p_0'{:}\ln s^*$ plane and the bottom one, the mechanical response in the $S_r{:}\ln p^*$ plane. The initial position of each yield curve is indicated by a solid line whereas, if yielding occurs, the corresponding final positions of the yield curves are indicated by chain-dotted lines. Arrows indicate the movement of the stress point and the shaded zone indicates other possible positions of the final stress point that would also activate the same type of model response. For clarity, the responses are shown for isotropic stress conditions, but equivalent conclusions apply in general stress space.

Figure 5a shows an example of purely elastic behaviour (STRPTH=1) and corresponds to a situation where the final stress point remains inside the elastic domain (i.e. $f_{\mathrm{WR}} \leq FTOL$ & $f_{\mathrm{DR}} \leq FTOL$ & $f_{\mathrm{M}} \leq FTOL$, where $FTOL$ is a specified tolerance) so that all yield curves remain at the same initial position. In contrast, Figures 5b and 5c show typical responses for retention yielding alone (STRPTH=2 or 3) causing plastic changes of S_r. Note that in each of these two cases the retention curve not being yielded has also moved from its initial position as a consequence of the associated movement defined by Equation 21. No plastic straining occurs when STRPTH=2 or 3 because the stress path remains inside f_{M} (Figures 5b and5c). As a consequence, the saturated mechanical yield stress p_0' remains unchanged (and, hence, the mechanical yield curve does not move).

Figure 5d shows an example of yielding on only f_{M} (STRPTH=4) where only the mechanical yield curve moves from its initial position as a consequence of plastic straining. Examples of yielding on two yield curves simultaneously are illustrated in Figures 5e and 5f. In these, plastic straining and plastic changes of S_r occur at the same time and, as a result, all yield curves move.

The forms of Equation 8 (for the mechanical response) and Equations 18 and 20 (for water retention response) plotted in Figure 5 demonstrate one of the computational advantages of the reformulated equations of the GCM discussed earlier. Equation 8, for example, corresponds to the integrated form of how the coupling of the water retention behaviour on the mechanical response is represented within the GCM. Similarly, Equations 18 and 20, correspond to the integrated form of the coupling of the mechanical response on the water retention. As further demonstrated later, these integrated forms of the couplings between mechanical and retention responses facilitate the identification of the active model response and simplify the intersection problem arising when a stress path crosses a yield curve of the model.

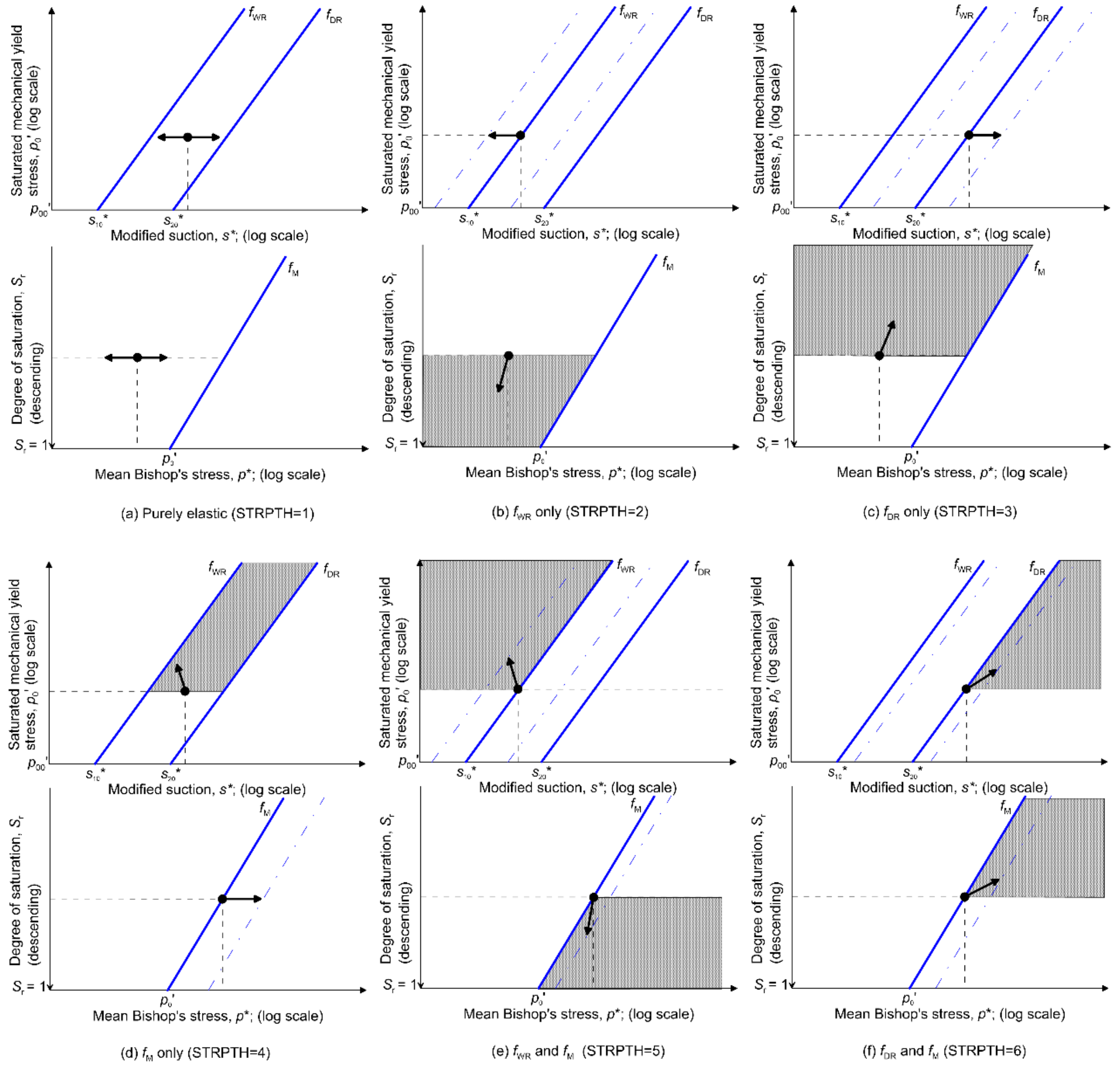

Figure 5 Typical model responses for isotropic stress states under unsaturated conditions.

3. MECHANICAL AND WATER RETENTION RELATIONS

When using the finite element method in problems involving saturated soils that may eventually desaturate, the *local* (i.e. within the element) integration of the coupled constitutive model representing the material behaviour of the soil involves the solution of both the mechanical and water retention incremental relations. During a typical finite element iteration in such problems, the nodal displacement and pore fluid pressures (including water and air) increments are usually found from the solution of the discretized *global* system of equations, typically involving equilibrium and mass balance relations (e.g. Olivella et al., 1996). Nodal displacement increments are combined with the strain-displacement relations to find the corresponding strain increments at a finite number of Gauss points within each element and, similarly, nodal pore fluid pressures increments are combined to find the corresponding increment of suction at each Gauss point. The known strain and suction increments can be then used at the local level to find the corresponding increments of stresses and degree of saturation via integration of the coupled constitutive model. It is hence convenient in finite element analysis (FEA) to express the local integration algorithm in terms of the *known* strain and suction increments (i.e. strain-driven algorithm). Because of their compatibility in FEA, this section focuses on strain-driven formulations to integrate the constitutive relations of the GCM, extending to unsaturated conditions the work on explicit substepping algorithms with automatic error control proposed in Sloan et al. (2001) for saturated soils.

3.1. Formulation of the problem

The numerical integration of a constitutive model for unsaturated soils involves the solution of an initial value problem (IVP) defined by the incremental relationships of the model, the initial (or current) state, the corresponding parameters of the model and, in the context of strain-driven formulations, a given pair of $\Delta\boldsymbol{\varepsilon}$ and Δs (Δ denotes a finite variation). Expressing the relations of the GCM by means of a strain-driven formulation is very convenient because, irrespective of the model response active, Δs^* can be computed correctly from the initial (or current) state at i and the exact updates of specific volume v and matric suction s at i+1:

$$^{i+1}s = {}^{i}s + \Delta s \tag{31}$$

$$^{i+1}v = {}^{i}v \exp\left(-\Delta\varepsilon_{\mathrm{v}}\right) \tag{32}$$

The correct update of s^* at i+1 is then given by:

$$^{i+1}s^* = {}^{i+1}s \frac{^{i+1}v - 1}{^{i+1}v} \tag{33}$$

From where the correct increment of modified suction can be calculated:

$$\Delta s^* = {}^{i+1}s^* - {}^{i}s^* \tag{34}$$

Once the increments of modified suction are known, the remaining incremental quantities can be expressed in a general IVP form as follows. The first two equations describe the mechanical response (Bishop's stress – strain relations) and the second pair the water retention response (modified suction – degree of saturation relations):

$$\Delta\boldsymbol{\sigma}^* = \mathbf{D_e}\Delta\boldsymbol{\varepsilon} - \Delta\lambda_{\mathrm{M}}\mathbf{D_e}\mathbf{a_M} \tag{35}$$

$$\Delta p_0' = \Delta\lambda_M B_M \tag{36}$$

$$\Delta S_r = -\Delta\lambda_R a_R \tag{37}$$

$$\Delta s^*_{R0} = -\Delta\lambda_R B_R \tag{38}$$

where the subscript M indicates mechanical response and the subscript R indicates retention response (with 1 for f_{WR} and 2 for f_{DR}), $\Delta\lambda_M$ and $\Delta\lambda_R$ are the respective plastic multipliers, p_0' and s^*_{R0} are the respective hardening parameters, $\mathbf{a_M}$ is the gradient of the mechanical yield curve with respect to Bishop's stress, a_R is the derivative of the retention yield curve with respect to modified suction, B_M is a scalar function for the mechanical response and B_R is a scalar function for the retention response.

3.1.1. Elastic behaviour

Elastic behaviour under saturated or unsaturated conditions (STRPTH=1) is a particular case of the general problem defined by Equations 35-38, noting that for STRPTH=1, the mechanical and retention plastic multipliers are both zero.

Elastic behaviour is represented in the GCM in terms of the secant bulk $\bar{K}$ and shear $\bar{G}$ moduli, equivalent to saturated soils (Sheng et al., 2000). This representation ensures the correct computation of Bishop's stresses at the intersection of the stress path with one of the three yield curves of the model, when the computed response passes from elastic to plastic. Integrating Equation 4 for p^* and ε_v^e the following analytical expression for $\bar{K}$ can be found (Lloret-Cabot et al., 2016):

$$\bar{K} = \frac{{}^i p^*}{\Delta\varepsilon_v^e}\left[\exp\left(\frac{{}^i v\left(1-\exp\left(-\Delta\varepsilon_v^e\right)\right)}{\kappa}\right)-1\right] \tag{39}$$

where ${}^i p^*$ and ${}^i v$ are, respectively, the mean Bishop's stress and specific volume at the start of the volumetric strain increment i. A corresponding appropriate expression for $\bar{G}$ should also be used (the form of this will depend upon what assumption is made for the tangent shear modulus G, see Potts and Zdravkovic, 1999).

3.1.2. Elasto-plastic behaviour

Equations 35-38 are valid for all types of elasto-plastic yielding, including unsaturated and saturated conditions, noting that, under saturated conditions, increases of S_r are prevented.

Some useful simplifications are possible for the particular cases of yielding on one water retention curve alone (STRPTH=2 or 3). Due to the absence of mechanical yielding, p_0' remains unchanged which means that the mechanical plastic multiplier is zero and then the increment of Bishop’s stress can be computed exactly, using the approach discussed for the elastic case. Also, given that $\Delta\lambda_{\mathrm{M}} = 0$, it is possible to compute exact values of degree of saturation at the updated exact value of modified suction (Equation 33) using Equation 25 for yielding on only f_{WR} or Equation 26 for yielding on only f_{DR}.

For mechanical yielding alone (STRPTH=4), whether the soil is saturated or unsaturated, $\Delta\lambda_{\mathrm{R}} = 0$ because $\Delta S_r = 0$. This means that the expression for $\Delta\lambda_{\mathrm{M}}$ can be found in the same way as that of the plastic multiplier for the MCC (see Sloan et al., (2001) for details).

Hence, the only two mechanisms that require the derivation of a new expression for the mechanical and water retention plastic multipliers correspond to simultaneous yielding on f_{M} and f_{R} (STRPTH=5 or 6). When f_{M} and f_{R} yield simultaneously, it is necessary to impose the consistency condition on both to find expressions for $\Delta\lambda_{\mathrm{M}}$ and $\Delta\lambda_{\mathrm{R}}$ in terms of $\Delta\boldsymbol{\varepsilon}$ and Δs:

$$\mathrm{d}f_{\mathrm{M}} = 0 \;\Rightarrow\; \left(\frac{\partial f_{\mathrm{M}}}{\partial \boldsymbol{\sigma}^{*}}\right)^{T} \mathbf{D_e}\left(\Delta\boldsymbol{\varepsilon} - \Delta\boldsymbol{\varepsilon}^{\mathbf{p}}\right) + \frac{\partial f_{\mathrm{M}}}{\partial p_0^{*}}\left[\frac{\partial p_0^{*}}{\partial p'_0}\Delta p'_0 + \frac{\partial p_0^{*}}{\partial S_r}\Delta S_r\right] = 0 \qquad (40)$$

$$\mathrm{d}f_{\mathrm{R}} = 0 \;\Rightarrow\; \left(\frac{\partial f_{\mathrm{R}}}{\partial s^{*}}\right)\Delta s^{*} + \frac{\partial f_{\mathrm{R}}}{\partial s_{\mathrm{R}}^{*}}\left[\frac{\partial s_{\mathrm{R}}^{*}}{\partial s_{\mathrm{R0}}^{*}}\Delta s_{\mathrm{R0}}^{*} + \frac{\partial s_{\mathrm{R}}^{*}}{\partial p'_0}\Delta p'_0\right] = 0 \qquad (41)$$

General expressions for the mechanical and retention plastic multipliers can be found by solving simultaneously the above expressions, after inserting the relevant hardening laws (Equations 9 and 21) and the relevant flow rules (Equations 10 and 24):

$$\Delta\lambda_{\mathrm{M}} = \frac{\mathbf{D_M}\Delta\boldsymbol{\varepsilon} + C_{\mathrm{M}}\Delta s^{*}}{A + \mathbf{D_M}\mathbf{a_M}} \qquad (42)$$

$$\Delta\lambda_{\mathrm{R}} = \frac{D_{\mathrm{R}}\Delta s^{*} + \mathbf{C_R}\Delta\boldsymbol{\varepsilon}}{A + \mathbf{D_M}\mathbf{a_M}} \qquad (43)$$

where $\mathbf{D_M}$, D_{R}, C_{M}, $\mathbf{C_R}$ and A are given by:

$$\mathbf{D_M} = \mathbf{a}_{\mathbf{M}}^{T}\mathbf{D_e} \qquad (44)$$

$$D_{\mathrm{R}} = \frac{-1}{B_{\mathrm{R}}}\left(\mathbf{D_M a_M} - \frac{\partial f_{\mathrm{M}}}{\partial p_0^*}\frac{\partial p_0^*}{\partial p'_0} B_{\mathrm{M}}\right) \frac{\partial s_{\mathrm{R0}}^*}{\partial s_{\mathrm{R}}^*} \tag{45}$$

$$C_{\mathrm{M}} = \frac{1}{B_{\mathrm{R}}}\frac{\partial f_{\mathrm{M}}}{\partial p_0^*}\frac{\partial p_0^*}{\partial S_r}\frac{\partial s_{\mathrm{R0}}^*}{\partial s_{\mathrm{R}}^*}\frac{\partial f_{\mathrm{R}}}{\partial s^*} \tag{46}$$

$$\mathbf{C_R} = \frac{B_{\mathrm{M}}}{B_{\mathrm{R}}}\left[\frac{\partial s_{\mathrm{R0}}^*}{\partial s_{\mathrm{R}}^*}\frac{\partial s_{\mathrm{R}}^*}{\partial p_0'}\right]\mathbf{D_M} \tag{47}$$

$$A = -\left(1-k_1k_2\right)\frac{\partial f_{\mathrm{M}}}{\partial p_0^*}\frac{\partial p_0^*}{\partial p_0'}\, B_{\mathrm{M}} \tag{48}$$

The expressions for the scalar functions B_{M} and B_{R} are:

$$B_{\mathrm{M}} = \frac{\partial p_0'}{\partial \varepsilon_v^p}\frac{\partial f_{\mathrm{M}}}{\partial p^*} \tag{49}$$

$$B_{\mathrm{R}} = \frac{\partial s_{\mathrm{R0}}^*}{\partial S_r^p}\frac{\partial f_{\mathrm{R}}}{\partial s^*} \tag{50}$$

As noted earlier, Δs^* can be computed exactly when $\Delta\boldsymbol{\varepsilon}$ and Δs are known (Equation 34).

3.2. Algorithm for the identification of the model response

The reformulation of GCM has facilitated the development of an algorithm that identifies, unambiguously, which is the model response activated by the given increments $\Delta\boldsymbol{\varepsilon}$ and Δs. Once the model response is known, all variables are updated using the appropriate set of incremental relations derived in the previous section. In such update, the algorithm automatically checks if the stress path intersects a yield curve and, if so, finds the corresponding intersection by using the Pegasus algorithm proposed by Dowell and Jarratt (1972), and widely tested for saturated soil models (Sloan et al., 2001, Abbo, 1997, Sheng et al., 2000, Pedroso et al., 2008, Zhao et al., 2005).

Figure 6 illustrates the various steps carried out by the algorithm to decide how to integrate the given increments of $\Delta\boldsymbol{\varepsilon}$ and Δs correctly. The case illustrated corresponds to the most challenging scenario in which, from an initial point inside the elastic domain, the known increments $\Delta\boldsymbol{\varepsilon}$ and Δs end up activating yielding on two yield curves. The particular model response plotted corresponds to STRPTH=6, but equivalent results are obtained for STRPTH=5. A maximum of three different trials is needed to handle correctly this problem. This means that, in the worst situation, the algorithm needs to break $\Delta\boldsymbol{\varepsilon}$ and Δs in three parts. All other cases (i.e. initial stress point on one or two yield curves) are a simplified version of this one and, hence, follow the same logic.

Figure 6 is in two parts. Part a shows the full sequence of steps in the $\ln p_0'$:$\ln s^*$ plane whereas Part b illustrates their counterparts in the S_r:$\ln p^*$ plane (note that the values of S_r in the vertical axis increase downwards). The current stress point is indicated by i and is assumed to be inside the three yield curves of the model (note that ${}^{i}f_{\mathrm{WR}}$ is not included in Figure 6a for clarity, but its location is to the left of point i, see Figure 5 for reference). *Trial 1* (indicated by t_1) is purely elastic ($\Delta S_r = 0$ and $\Delta p_0' = 0$) and ends up outside both ${}^{i}f_{\mathrm{DR}}$ (see Figure 6a) and ${}^{i}f_{\mathrm{M}}$ (see Figure 6b). Hence, it is necessary to check which of these two yield curves is hit first by *trial 1*. This problem involves finding two scalars (α_1 for f_{DR} and α_2 for f_{M}), both between 0 and 1, that indicate the portion of $\Delta\boldsymbol{\varepsilon}$ and Δs required to move, elastically, the stress point i to the corresponding intersection point (indicated as i_{R1} for f_{DR} and i_{M1} for f_{M}). The lower value of the two scalars corresponds to the yield curve hit first by *trial 1*. In the example represented in Figure 6, f_{DR} is the yield curve hit first (i.e. $\alpha_1 < \alpha_2$). Hence, a purely elastic update of the stress point from i to the intersection point i_{R1} is then carried out using the appropriate portion of the given increments (i.e. $\alpha_1\Delta\boldsymbol{\varepsilon}$ and $\alpha_1\Delta s$). The next step is to compute *Trial 2* (indicated as t_2) starting from i_{R1} (also indicated as i_{R} in Figure 6) and now assuming yielding on only f_{DR}. Importantly, *Trial 2* uses only the not yet integrated part of the increments of strains and suction i.e. $(1\text{-}\alpha_1)\Delta\boldsymbol{\varepsilon}$ and $(1\text{-}\alpha_1)\Delta s$. Given that yielding on only f_{DR} is the model response assumed in computing t_2, the mechanical hardening parameter p_0' is constant (see Figure 6a) and the corresponding value of S_r is exact because it can be calculated inserting the exact value of modified suction at t_2 (which equals that calculated in t_1, see Figure 6a) in the equation of the main drying curve (Equation 26). A second intersection problem arises, now with ${}^{i}f_{\mathrm{M}}$ (Figure 6). This second intersection problem involves finding a scalar β (also between 0 and 1) that defines the portion of $(1\text{-}\alpha_1)\Delta\boldsymbol{\varepsilon}$ and $(1\text{-}\alpha_1)\Delta s$ required to move, under yielding on only f_{DR}, the stress point from i_{R} to i_{M} (also indicated as i_{Y} in Figure 6 to highlight that the stress point lies on both yield curves). Once β has been found, the stress point is updated from i_{R} to i_{M} assuming yielding on only f_{DR} and using the relevant portion of strain and suction increments i.e. $\beta(1\text{-}\alpha_1)\Delta\boldsymbol{\varepsilon}$ and $\beta(1\text{-}\alpha_1)\Delta s$. In moving the stress point from i_{R} to i_{M}, yielding on only f_{DR} is occurring and, consequently, ${}^{i}f_{\mathrm{DR}}$ yields to ${}^{\mathrm{Y}}f_{\mathrm{DR}}$ as indicated by the thicker light dashed line in Figure 6a. At this stage, the stress point is on both yield curves. A final *trial 3*, now assuming yielding on only f_M, needs to be computed to determine whether the portion not yet integrated of strains and suction increments (i.e. $(1-\beta)(1-\alpha_1)\Delta\boldsymbol{\varepsilon}$ and $(1-\beta)(1-\alpha_1)\Delta s$) activates yielding on only f_M or simultaneous yielding on f_M and f_{DR}. Conveniently, the algorithm *knows* at this point that yielding on only f_{DR} is not possible because *trial 2* fell outside f_M when assuming yielding on only f_{DR}. In the example of Figure 6, *trial 3* ends up outside ${}^{Y}f_{DR}$ meaning that this final portion of $\Delta\boldsymbol{\varepsilon}$ and Δs, moving the stress point from i_Y to i+1, has to be integrated assuming simultaneous yielding on f_M and f_{DR}. The stress path followed to integrate the full size of $\Delta\boldsymbol{\varepsilon}$ and Δs is indicated in the figure by a thick black solid line and the final positions of f_M and f_{DR} at i+1 are indicated by a lighter thick solid line.

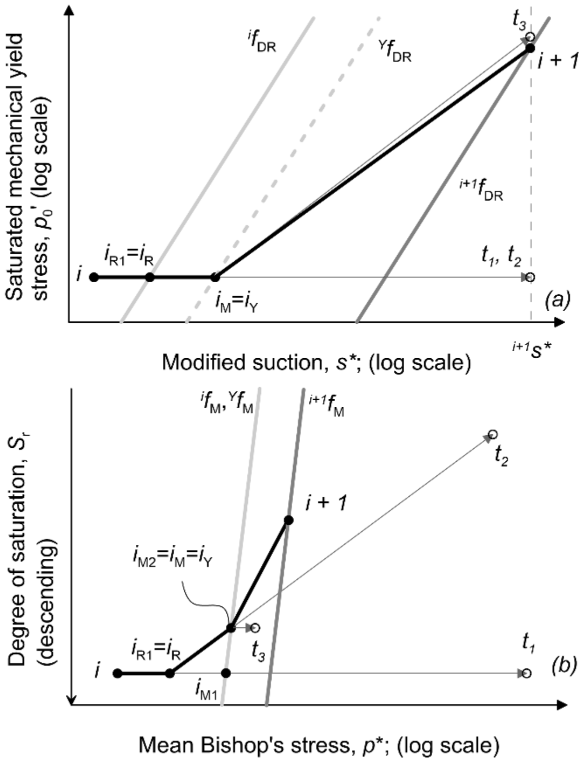

Figure 6 Example of a typical integration of the GCM starting from inside the three yield curves and ending up activating yielding on two yield surfaces (STRPTH=6).

A more formalised description of the sequence of steps followed by the algorithm to determine which is the active response of the GCM is presented in Appendix B.

3.3. Yield intersections

The given increments of $\Delta\boldsymbol{\varepsilon}$ and Δs may change the stress state from elastic to elasto-plastic within the increment. In the context of the GCM, this means that a *trial* intersects at least one yield curve. Note that during a transition from unsaturated to saturated conditions, there might also be the reverse situation (i.e. from elasto-plastic to elastic within an individual increment) in wetting paths that saturate during collapse compression (Lloret-Cabot et al., 2017, Lloret-Cabot et al., 2018) i.e. it is possible to have within a single increment a first part (while unsaturated) that is elasto-plastic and a second part (while saturated) that is elastic. The intersection point in such cases is controlled by the value of S_r but it is found in an equivalent way to any other intersection problem. All of these intersections are found here using the Pegasus algorithm proposed by Dowell and Jarratt (1972) and extensively used in the literature (e.g. Sloan et al., 2001, Abbo, 1997, Sheng et al., 2000, Pedroso et al., 2008, Zhao et al., 2005). Its algorithmic form is summarised in Appendix C for completeness).

There might situations in which the given increments of strain and suction intersect a yield surface twice, even though initial and final stress states are both inside the yield locus. Such situation is aggravated when using too large increments and, hence, the use of sufficiently small increments of strain and suction is recommended. Sołowski & Sloan (2012) discuss this intersection problem further in the context of the BBM (Alonso et al. 1990).

Another possible intersection problem is that referred to as “elasto-plastic unloading” (Sloan et al. 2001). The solution to this problem in the context of the GCM is equivalent to that proposed for critical state saturated models (e.g. Sloan et al., 2001, Abbo, 1997, Sheng et al., 2000, Pedroso et al., 2008).

3.4. Drift correction

Similarly to what is observed in explicit integration schemes for saturated soils, in unsaturated soils too the stress point at the end of each integration step/substep may *drift* from the yield condition, so that $|f_A| > FTOL$. The extent of this drift primarily depends on the accuracy of the integration scheme used and, in general, when using substepping strategies with error control, drift correction is rarely needed Sołowski et al. (2012). However, as advised in Sloan et al. (2001), it is prudent to consider the possibility to correct a potential drift at the end of each integrated step/substep.

In the context of the GCM, a correction of the drift of the stress point is only potentially needed when mechanical yielding occurs, whether this implies yielding on only f_M (STRPTH=4) or simultaneous yielding on f_M and a retention yield curve (STRPTH=5 or 6). Yielding on a retention yield curve alone (STRPTH=2 or 3) does not require any drift correction in the context of strain-driven formulations because, as explained earlier, an exact update of all relevant variables is possible.

The strategy to correct the stress point in the GCM adopts the drift correction method recommended in Potts and Gens (1984) for saturated soils. The extension of such strategy to unsaturated soils includes the assumption that, in addition to imposing no strain variations i.e. $\delta\boldsymbol{\varepsilon} = \mathbf{0}$ during the correction of the stress point, also suction remains unchanged i.e. $\delta s = 0$. The latter assumption has been successfully used for the numerical integration of many other unsaturated soil models (e.g. Sánchez et al. 2008, Sołowski and Gallipoli 2010ab).

Assuming $\delta\boldsymbol{\varepsilon} = \mathbf{0}$ and $\delta s = 0$ means that the correction of modified suction δs^* and specific volume δv are both zero. Given that $\delta s^* = 0$, the correction of degree of saturation δS_r and of the water retention hardening parameters δs_{R0}^* are all also zero. The correction of Bishop's stresses $\delta\boldsymbol{\sigma}^*$ and mechanical hardening parameter $\delta p_0'$ are unknown quantities and can be found by expanding f_M in Taylor series about the stress point to be corrected i. Neglecting second order terms and above, this can be expressed by:

$$f_M \approx {}^i f_M + {}^i\left(\frac{\partial f_M}{\partial \boldsymbol{\sigma}^*}\right)\delta\boldsymbol{\sigma}^* + {}^i\left(\frac{\partial f_M}{\partial p_0^*}\right)\left(\frac{\partial p_0^*}{\partial p_0'}\delta p_0' + \frac{\partial p_0^*}{\partial S_r}\delta S_r\right) \tag{51}$$

where $\delta S_r = 0$.

Equations 35 and 36 mean that for the total strain increment to remain zero, the corrections in the Bishop's stress and mechanical hardening parameter are, respectively:

$$\delta\boldsymbol{\sigma}^* = -\delta\lambda_M \mathbf{D_e a_M} \tag{52}$$

$$\delta p_0' = \delta\lambda_M B_M \tag{53}$$

where $\delta\lambda_M$ is an unknown multiplier and $\mathbf{D_e}$, $\mathbf{a_M}$ and B_M are all evaluated at i.

The following expression for $\delta\lambda_M$ is found by combining Equations 51-53, after imposing that $f_M = 0$:

$$\delta\lambda_{\mathrm{M}} = \frac{f_{\mathrm{M}}}{\mathbf{a}^T\mathbf{D_e}\mathbf{a} - \frac{\partial f_{\mathrm{M}}}{\partial p_0^*}\frac{\partial p_0^*}{\partial p_0'}B_{\mathrm{M}}} \tag{54}$$

While there is no need to correct s^*, $s_{\mathrm{R}0}{}^*$, S_r nor v, a correction needs to be applied to the mechanical and the water retention yield stresses:

$$\delta p_0^* = \frac{p_0^*}{p_0'}\delta\lambda_{\mathrm{M}} B_{\mathrm{M}} \tag{55}$$

$$\delta s_{\mathrm{R}}^* = k_2 \frac{s_{\mathrm{R}}^*}{p_0'}\delta\lambda_{\mathrm{M}} B_{\mathrm{M}} \tag{56}$$

where all variables are evaluated at i.

4. EXPLICIT SUBSTEPPING INTEGRATION SCHEMES

This section presents two explicit substepping integration schemes for the numerical integration of the GCM. The first one corresponds to the second order accurate modified Euler with substepping (ME2) whereas the second one is the fifth order accurate Runge-Kutta-Dormand-Prince (RKDP5) with substepping. The notation adopted extends that employed by Sloan et al. (2001) to unsaturated soils, making explicit the dependence of the initial value problem (IVP) on the specific volume (as in critical state models for saturated soils, see Lloret-Cabot et al., 2016) and also on the degree of saturation. A comparative analysis of the relative numerical performance of these two substepping integration schemes is provided in the next section.

For the same reasons given in the drift correction approach, the application of a substepping strategy with error control in the GCM is unnecessary in absence of mechanical yielding, whether this means elastic behaviour or yielding on only one retention curve (i.e. STRPTH=1, 2 or 3). In contrast, a substepping strategy with error control becomes extremely convenient for the numerical integration of the incremental relations of the GCM when mechanical yielding is active, because for STRPTH=4, 5 or 6 the incremental constitutive laws are not integrable analytically. In such cases, the key to ensure an accurate and efficient numerical integration is to control the local error in the computed variables arising due to the inexact integration of the integration scheme. In a substepping integration scheme, this local error is controlled by using a measure of the truncation error, which is estimated as the difference between the approximate solutions from two integration schemes of different order (Shampine, 1994). How much these two approximations differ from each other is indicative of the deviation of the numerical solution from the true solution and, hence, this difference can be used to estimate the truncation error and to automatically adjust, then, the size of the current integration step/substep.

To extend to unsaturated conditions the formulation of Sloan et al. (2001) presented for saturated soils, it is useful to express the equations involved in the problem in terms of a pseudo-time T:

$$T = \frac{t - {}^{i=0}t}{\Delta t} \tag{57}$$

where $t = {}^{i=0}t$ is the time at the start of the strain increment $\Delta\boldsymbol{\varepsilon}$ and suction increment Δs (i.e. $T = 0$), $t = {}^{0}t + \Delta t$ is the time at the end of the strain and suction increments (i.e. $T = 1$) and $0 \leq T \leq 1$.

$$\frac{\mathrm{d}s}{\mathrm{d}T} \cong \Delta s \tag{58}$$

$$\frac{\mathrm{d}v}{\mathrm{d}T} \cong v\exp\left(-\Delta\varepsilon_{\mathrm{v}}\right) \tag{59}$$

$$\frac{\mathrm{d}s^{*}}{\mathrm{d}T} \cong \Delta s^{*} \tag{60}$$

$$\frac{\mathrm{d}\boldsymbol{\sigma}^{*}}{\mathrm{d}T} \cong \Delta\boldsymbol{\sigma}^{*} = \mathbf{D_e}\Delta\boldsymbol{\varepsilon} - \Delta\lambda_{\mathrm{M}}\mathbf{D_e}\mathbf{a_M} \tag{61}$$

$$\frac{\mathrm{d}p_0'}{\mathrm{d}T} \cong \Delta p_0' = \Delta\lambda_{\mathrm{M}}B_{\mathrm{M}} \tag{62}$$

$$\frac{\mathrm{d}S_r}{\mathrm{d}T} \cong \Delta S_r = -\Delta\lambda_{\mathrm{R}}a_{\mathrm{R}} \tag{63}$$

$$\frac{\mathrm{d}s^{*}_{\mathrm{R0}}}{\mathrm{d}T} \cong \Delta s^{*}_{\mathrm{R0}} = \Delta\lambda_{\mathrm{R}}B_{\mathrm{R}} \tag{64}$$

where the subscript "$_{\mathrm{R}}$" is 1 for f_{WR} and 2 for f_{DR}.

The system of Equations 58-64 defines an initial value problem (IVP) that can be integrated over T knowing the values at the initial (or current) state i of modified suction ${}^{i}s^{*}$, Bishop's stress ${}^{i}\boldsymbol{\sigma}^{*}$, hardening parameters ${}^{i}p_0'$ and ${}^{i}s_{\mathrm{R0}}{}^{*}$, specific volume ${}^{i}v$ and degree of saturation ${}^{i}S_r$, together with the imposed $\Delta\boldsymbol{\varepsilon}$ and Δs. Similarly to the strain-driven numerical integration of the MCC for $\Delta\boldsymbol{\varepsilon}$, also Δs is fixed in the strain-driven integration of the GCM presented here, meaning that the IVP is solved assuming constant strain and suction rates, $\Delta\boldsymbol{\varepsilon}/\Delta t$ and $\Delta s/\Delta t$, during each step/substep.

The form of the system of equations 59-64 is a direct consequence of assuming that not only the mechanical behaviour of unsaturated soils can be represented as an elasto-plastic process but also the water retention response (Wheeler et al. 2003). Under these considerations, the system of equations 59 to 64 encompasses saturated and unsaturated conditions and incorporates the coupling between the mechanical and the water retention behaviour. Although the specific GCM equations are used, the same integration scheme is applicable to any model that, in addition to assuming elasto-plastic formulations for the mechanical and the water retention responses, accounts for the coupling between mechanical and water retention behaviour via plastic volumetric strains and plastic changes of degree of saturation.

A substepping integration scheme integrates the incremental relations of a constitutive model by automatically adjusting the size of the given integration interval (or increment) depending on a relative measure of the local error, *REL*. When *REL* is larger/smaller than a specified tolerance (i.e. *STOL*), the current size of the integration step/substep is reduced/increased according to ${}^{i+1}(\Delta T)=r\,{}^{i}(\Delta T)$ where the scalar r is estimated as follows. Based on the assumption that the size of a step/substep varies proportionally to a measure of the local error r, Sloan et al. (2001) suggest to use $r \cong 0.9(STOL/REL_n)^{1/2}$ for the second order accurate modified Euler with substepping and $r \cong 0.9(STOL/REL_n)^{1/5}$ for the fifth order accurate Runge-Kutta-Dormand-Prince with substepping. An additional constraint for the scalar r is to bound its values between 0.1 and 1.1 to limit the change in size during two consecutive substeps, and a maximum number of substeps needs to be also specified (see Sloan et al. (2001) for full details).

A major point of the substepping integration schemes presented here is that the measure of the relative error *REL* is estimated for $\boldsymbol{\sigma}^*$, p_0', S_r and s_{R0}^*. The reason for treating these variables separately is because the estimated values of the respective local error for mechanical ($\boldsymbol{\sigma}^*$ and p_0') and water retention responses (S_r and s_{R0}^*) can have different magnitudes. Hence, it is important for an efficient integration of a problem involving unsaturated soils that when substepping integration schemes with automatic error control are used, the error measure *REL* is estimated accounting for all major sources of error, and for unsaturated soils these should include the local error arising during the numerical integration of both mechanical and water retention constitutive relations. In the two substepping integration schemes presented here, this measure of relative local error *REL* is estimated by taking the difference between the higher order accurate and the lower order accurate approximations for $\boldsymbol{\sigma}^*$, p_0', S_r and s_{R0}^*. Each of these differences is then divided by the corresponding higher order approximation (indicated by a hat in Equation 65). For the modified Euler with substepping this corresponds to the difference between second order accurate modified Euler and first order accurate forward Euler. For the RKDP5 with substepping, *REL* is calculated from fourth and fifth Runge-Kutta-Dormand-Prince approximations.

Equivalently to what is proposed in Sloan et al. (2001) for saturated soils, *REL* takes the maximum of these four relative measures of the step/substep error as a way to bound the local error:

$$REL = max\left\{ \frac{\left[\left(\hat{\boldsymbol{\sigma}}^* - \boldsymbol{\sigma}^*\right)^T \left(\hat{\boldsymbol{\sigma}}^* - \boldsymbol{\sigma}^*\right)\right]^{1/2}}{\left[\left(\hat{\boldsymbol{\sigma}}^*\right)^T \left(\hat{\boldsymbol{\sigma}}^*\right)\right]^{1/2}}, \frac{\left|\hat{p}_0' - p_0'\right|}{\hat{p}_0'}, \frac{\left|\hat{S}_r - S_r\right|}{\hat{S}_r}, \frac{\left|\hat{s}_{R0}^* - s_{R0}^*\right|}{\hat{s}_{R0}^*} \right\} \qquad (65)$$

4.1. Modified Euler with substepping

Given a pseudo-time step/substep ${}^i(\Delta T)$ with $0 < {}^i(\Delta T) \leq 1$, the forward Euler and modified Euler updates for $\boldsymbol{\sigma}^*$, p_0', S_r and s_{R0}^* are described in the following by adopting the Butcher tableau (Dormand and Prince, 1980). The coefficients for the two methods are summarised in Table 1. The subscripts i and i+1 denote quantities evaluated at pseudo-times ${}^iT$ and ${}^{i+1}T = {}^iT + {}^i(\Delta T)$ respectively:

$${}^{i+1}s = {}^i s + {}^i \Delta s \qquad (66)$$

$${}^{i+1}v = {}^i v \exp\left(-{}^i \Delta\varepsilon_v\right) \qquad (67)$$

$${}^{i+1}s^* = {}^{i+1}s \frac{{}^{i+1}v - 1}{{}^{i+1}v} \qquad (68)$$

$${}^{i+1}\boldsymbol{\sigma}^* = {}^i\boldsymbol{\sigma}^* + \sum_{k=1}^{n_s} {}^k b \, {}^k \Delta\boldsymbol{\sigma}^* \qquad (69)$$

$${}^{i+1}p_0' = {}^i p_0' + \sum_{k=1}^{n_s} {}^k b \, {}^k \Delta p_0' \qquad (70)$$

$$ {}^{i+1}S_r = {}^{i}S_r + \sum_{k=1}^{n_s} {}^{k}b\, {}^{k}\Delta S_r \tag{71} $$

$$ {}^{i+1}s^*_{\mathrm{R0}} = {}^{i}s^*_{\mathrm{R0}} + \sum_{k=1}^{n_s} {}^{k}b\, {}^{k}\Delta s^*_{\mathrm{R0}} \tag{72} $$

where the coefficients ${}^{k}b$ are summarised in Table 1, n_s is the number of stages of the integration scheme, and

$$ \left. \begin{aligned} {}^{k}\Delta s^* &= {}^{i+1}s^* - {}^{i}s^* \\ {}^{k}\Delta\boldsymbol{\sigma}^* &= {}^{k}\mathbf{D_e}\, {}^{i}\Delta\boldsymbol{\varepsilon} - {}^{k}\Delta\lambda_{\mathrm{M}}\, {}^{k}\mathbf{D_e}\, {}^{k}\mathbf{a_M} \\ {}^{k}\Delta p_0' &= {}^{k}\Delta\lambda_{\mathrm{M}}\, {}^{k}B_{\mathrm{M}} \\ {}^{k}\Delta S_r &= -{}^{k}\Delta\lambda_{\mathrm{R}}\, a_{\mathrm{R}} \\ {}^{k}\Delta s^*_{\mathrm{R0}} &= {}^{k}\Delta\lambda_{\mathrm{R}}\, {}^{k}B_{\mathrm{R}} \\ {}^{i}\Delta s &= {}^{i}(\Delta T)\Delta s \\ {}^{i}\Delta\boldsymbol{\varepsilon} &= {}^{i}(\Delta T)\Delta\boldsymbol{\varepsilon} \end{aligned} \right\} \quad \text{for } k = 1, \ldots n_s \tag{73} $$

where $\mathbf{D_e}$, $\mathbf{a_M}$, $\Delta\lambda_{\mathrm{M}}$, $\Delta\lambda_{\mathrm{R}}$, B_{M} and B_{R} are evaluated at k using:

$$ \left. \begin{aligned} {}^{k}\hat{s} &= {}^{i}s + \sum_{j=1}^{k-1} {}^{kj}a\, {}^{i}(\Delta T)\Delta s \\ {}^{k}\hat{v} &= {}^{i}v \exp\left(-\sum_{j=1}^{k-1} {}^{kj}a\, {}^{i}(\Delta T)\Delta\varepsilon_v \right) \\ {}^{k}\hat{s}^* &= {}^{k}\hat{s}\, \frac{{}^{k}\hat{v} - 1}{{}^{k}\hat{v}} \\ {}^{k}\hat{\boldsymbol{\sigma}}^* &= {}^{i}\boldsymbol{\sigma}^* + \sum_{j=1}^{k-1} {}^{kj}a\, {}^{j}\Delta\boldsymbol{\sigma}^* \\ {}^{k}\hat{p}_0' &= {}^{i}p_0' + \sum_{j=1}^{k-1} {}^{kj}a\, {}^{j}\Delta p_0' \\ {}^{k}\hat{S}_r &= {}^{i}S_r + \sum_{j=1}^{k-1} {}^{kj}a\, {}^{j}\Delta S_r \\ {}^{k}\hat{s}^*_{\mathrm{R0}} &= {}^{i}s^*_{\mathrm{R0}} + \sum_{j=1}^{k-1} {}^{kj}a\, {}^{j}\Delta s^*_{\mathrm{R0}} \end{aligned} \right\} \quad \text{for } k = 1, \ldots, n_s \tag{74} $$

and the coefficients ${}^{kj}a$ are summarised in Table 1.

Lloret-Cabot et al. (2016) demonstrate, for critical state models for saturated soils, the importance of ensuring that the update of v is consistent (i.e. at the same integration portion of $\Delta\boldsymbol{\varepsilon}$) with the update of effective stresses $\boldsymbol{\sigma}'$ and hardening parameter p_0'. An equivalent logic applies to integration of critical state models for unsaturated soils that account for mechanical and water retention behaviour where not only v, but also S_r needs to be updated rigorously (i.e. now at the same integration portion of both $\Delta\boldsymbol{\varepsilon}$ and Δs) with the update of $\boldsymbol{\sigma}^*$, s^*, p_0' and s_{R0}^* (Equation 74).

Strain-driven formulations allow for the exact computation of specific volume, matric suction and modified suction at the end of the step/substep because it is possible to integrate them analytically over ${}^{i}\Delta T$ to find the precise values of v, s and s^* at i+1. The corresponding second order accurate updates for $\boldsymbol{\sigma}^*$, p_0', S_r and s_{R0}^* are respectively given by Equations 69-72 where ${}^{1}\Delta\boldsymbol{\sigma}^*$, ${}^{1}\Delta p_0'$, ${}^{1}\Delta S_r$ and ${}^{1}\Delta s_{R0}^*$ correspond to the forward Euler increments and, ${}^{2}\Delta\boldsymbol{\sigma}^*$, ${}^{2}\Delta p_0'$, ${}^{2}\Delta S_r$ and ${}^{2}\Delta s_{R0}^*$ are computed using first order updated variables (see Equations 73 and 74). If the step/substep is accepted, the variables $\boldsymbol{\sigma}^*$, p_0', S_r and s_{R0}^* are updated using the higher order approximation (i.e. *local extrapolation* see Shampine, 1994).

Table 1. Coefficients for the forward Euler and modified Euler integration schemes (Dormand and Prince, 1980)

${}^{k}c$	${}^{kj}a$					${}^{k}\hat{b}$ (2nd)	${}^{k}b$ (1st)
0						1/2	1
1	1					1/2	0

4.2. Runge-Kutta-Dormand-Prince (RKDP) with substepping

The explicit Runge-Kutta-Dormand-Prince (RKDP) with substepping is applied here to integrate the mechanical and water retention relations of the GCM for STRPTH= 4, 5 and 6. When applying this scheme to Equations 58-64, the same Equations 66-74 are obtained but, for this method, the coefficients ${}^{k}b$ and ${}^{kj}a$ correspond to those summarised in Table 2.

The RKDP scheme with substepping gives very accurate values for ${}^{i+1}\boldsymbol{\sigma}^*$, ${}^{i+1}p_0'$, ${}^{i+1}S_r$ and ${}^{i+1}s_{R0}^*$ at the end of each step/substep, at the expense of additional evaluations of the constitutive relations. In the absence of an analytical solution, these highly accurate approximations are used as a *reference* to check the accuracy of lower order methods.

Table 2. Coefficients for the RKDP4 and RKDP5 integration schemes (Dormand and Prince, 1980)

${}^{k}c$	${}^{kj}a$					${}^{k}\hat{b}$ (5^{th})	${}^{k}b$ (4^{th})
0						19/216	31/540
1/5	1/5					0	0
3/10	3/40	9/40				1000/2079	190/297
3/5	3/10	-9/10	6/5			-125/216	-145/108
2/3	226/729	-25/27	880/729	55/729		81/88	351/220
1	-181/270	5/2	-266/297	-91/27	189/55	5/56	1/20

5. VERIFICATION AND COMPUTATIONAL ASPECTS

The variation of the local error with the size of the integrated increments depends on the order of local accuracy of the numerical method used. Based on this information, Lloret-Cabot et al. (2016) propose a verification method for the numerical integration of constitutive models for saturated soils. This verification strategy is especially convenient for explicit substepping integration schemes, because it first checks the expected behaviour of the error at the level of one single step/substep and it then checks the theoretical response of the cumulative error over several substeps.

As demonstrated here, the same strategy can be adapted to study the behaviour of the error in the numerical integration of models for unsaturated soils. In the development presented hereafter, e refers to the error incurred by the numerical scheme in a single substep (or step in the case of no substepping) and E is the cumulative error over a number of substeps. Note that the error control in a substepping strategy only controls the error in a single substep, with the aim of controlling the cumulative error over several steps.

To study the behaviour of the local error when numerically integrating a model, it is useful to compare the approximations given by the integration scheme against a reference or, when possible, an analytical solution. Given that the GCM involves mechanical and water retention behaviour, it is necessary to study the magnitude of the error not only in the mechanical response (as shown in Lloret-Cabot et al. (2016) for the saturated MCC) but also in the water retention response. Consequently, the assessment of the error investigated here for the integration of the GCM will include the relative error incurred in the approximated mechanical response (in terms of Bishop’s stresses $\boldsymbol{\sigma}^*$ and mechanical hardening parameter p_0') and the approximated water retention response (in terms of degree of saturation S_r and a water retention hardening parameter s_{R0}^*) when varying the size of $\Delta\boldsymbol{\varepsilon}$, Δs or both. The relative error in each of these variables in a single substep/step is computed as:

$$e_{\boldsymbol{\sigma}^*} = \frac{\left\{\left(\boldsymbol{\sigma}^*_{ref} - \boldsymbol{\sigma}^*\right)^T \left(\boldsymbol{\sigma}^*_{ref} - \boldsymbol{\sigma}^*\right)\right\}^{1/2}}{\left\{\left(\boldsymbol{\sigma}^*_{ref}\right)^T \left(\boldsymbol{\sigma}^*_{ref}\right)\right\}^{1/2}} \tag{75}$$

$$e_{S_r} = \frac{\left|S_{rref} - S_r\right|}{S_{rref}} \tag{76}$$

$$e_{p'_0} = \frac{\left|p'_{0ref} - p'_0\right|}{p'_{0ref}} \tag{77}$$

$$e_{s^*_{R0}} = \frac{\left|s^*_{R0ref} - s^*_{R0}\right|}{s^*_{R0ref}} \tag{78}$$

where the subscript *ref* indicates a reference solution (or, when available, analytical).

5.1. Relative error in a single-step

Two numerical tests are carried out to study how the error in $\boldsymbol{\sigma}^*$, S_r, p_0' and s_{R0}^* propagates during a single integration step (i.e. with no substepping) using the second order modified Euler (ME2) and the fifth order Runge-Kutta-Dormand-Prince (RKDP5) integration schemes. Both tests assume axisymmetric conditions and consider an initial unsaturated stress state lying on both mechanical and wetting retention yield curves, at zero deviatoric stress. The soil constants and initial state considered in all the simulations are summarised in Tables 3 and 4, respectively. This initial state gives initial values of specific volume and degree of saturation v = 2.20, S_r = 0.65. Further details on model parameters and initial state of GCM are found in Lloret-Cabot et al.

(2017). The tolerance associated with yield surface intersections and the correction of the stresses back to the yield curve, *FTOL*, is assumed equal to 10^{-12}.

Table 3. Values of soil constants for the GCM simulations for Tests A, B and C

$\lambda = 0.15$	$\kappa = 0.02$	$\mathrm{N} = 2.73$	$R = 1.4$	$\mathrm{M} = 1.20$
$\mathrm{N}^* = 2.90$	$k_1 = 0.70$	$k_2 = 0.80$	$\lambda_s = 0.12$	$\upsilon = 0.33$ (*)

(*) where υ is the Poisson's ratio (tangent and secant values of shear modulus were calculated from the corresponding tangent and secant values of bulk modulus by assuming a constant value of Poisson's ratio.

Table 4. Initial state for GCM simulations for Tests A and B (see the Appendix A)

$p^* = 200\,\mathrm{kPa}$	$q = 0\,\mathrm{kPa}$	$p_0^* = 200\,\mathrm{kPa}$
$s^* = 109.09\,\mathrm{kPa}$	--	$s_1^* = 109.09\,\mathrm{kPa}$

The reason for considering this type of initial state (with $p^* = p^*_0$ and $s^* = s_1{}^*$) is because when positive increments of strain (loading) and/or decrements of matric suction (wetting) are applied from the assumed initial state, simultaneous yielding on the mechanical and wetting retention yield curves (STRPTH=5) is activated which corresponds to the desired situation in which the numerical approximation of all four variables investigated contain some amount of error.

The first numerical test (Test A) studies the variation of the error for given finite equal variations of axial strain and radial strain $\Delta\varepsilon_a = \Delta\varepsilon_r \approx \Delta\varepsilon_v/3$ (where $\Delta\varepsilon_v$ is the increment of volumetric strain) with no variation of suction (i.e. isotropic straining at constant suction). The second test (Test B) studies the error response for a combined axial strain increment $\Delta\varepsilon_a$ (with no radial strains, $\Delta\varepsilon_r$) and a finite decrement of suction $-\Delta s$ (i.e. axial straining under wetting).

Test A computes the error by comparing the numerical approximation against the corresponding analytical solution. This comparison provides, hence, a clear and unambiguous interpretation of the error results. Conversely, Test B compares the numerical approximation against a reference solution (obtained by using the RKDP scheme with substepping and very stringent tolerances). In the two numerical tests presented, the size of the assumed input increments of strains and suction are varied to study how such variation in size influences the error in the solution. For Test A, the volumetric strain increment size analysed varies from $\Delta\varepsilon_v = 10^{-06}$ to 0.1 (with $\Delta s = 0$).

For Test B, the increment sizes varied from $\Delta\varepsilon_a = 10^{-06}$ and $\Delta s = -10^{-06}$ kPa to $\Delta\varepsilon_a$ = 0.01 and $\Delta s = -0.01$kPa (keeping $\Delta\varepsilon_r = 0$).

Accuracy in each numerical method is assessed by plotting the error in $\boldsymbol{\sigma}^*$, S_r, p_0' and s_{10}^* against the size of the input of strain or suction variations using logarithmic scales. This form of plotting the error results provides a first form of verification of an integration scheme, because the gradient obtained for the best-fitted straight line through a particular set of error results (i.e. all belonging to approximations from the same integration scheme) should be in correspondence with the order of accuracy of the numerical integration method (Lloret-Cabot et al., 2016).

Figures 7 and 8 illustrate the behaviour of the relative error for Tests A and B respectively, for a single step. Each figure is in four parts. The response of the relative error for the mechanical behaviour is shown in Parts (a) and (c), in terms of Bishop's stress $\boldsymbol{\sigma}^*$ and mechanical hardening parameter p_0', respectively. Parts (b) and (d) show the response of the relative error for the water retention behaviour in terms of degree of saturation S_r and wetting retention hardening parameter s_{10}^*, respectively. In the figures, symbols indicate the computed relative error and the dashed lines indicate the best-fitted straight line through the computed relative error for the same numerical method. Typical error results for Test A when using the ME2 and RKDP5 schemes, respectively, are summarised in Tables 5 and 6.

Table 5. Typical relative error values in Bishop's stress $\boldsymbol{\sigma}^*$, degree of saturation S_r, mechanical hardening parameter p_0' and wetting retention hardening parameter s_{10}^* for a single elasto-plastic isotropic loading step at constant suction for the modified Euler with substepping (ME2) considering *STOL* = 1.

$\Delta\varepsilon_v$	Error in $\boldsymbol{\sigma}^*$	Error in S_r	Error in p_0'	Error in s_{10}^*
$1\cdot10^{-06}$	$< 1.0\cdot10^{-15}$	$< 1.0\cdot10^{-15}$	$< 1.0\cdot10^{-15}$	$< 1.0\cdot10^{-15}$
$1\cdot10^{-05}$	$4.50\cdot10^{-14}$	$< 1.0\cdot10^{-15}$	$6.74\cdot10^{-13}$	$5.41\cdot10^{-13}$
$1\cdot10^{-04}$	$4.37\cdot10^{-11}$	$2.15\cdot10^{-13}$	$6.72\cdot10^{-10}$	$5.38\cdot10^{-10}$
$1\cdot10^{-03}$	$4.35\cdot10^{-08}$	$2.14\cdot10^{-10}$	$6.64\cdot10^{-07}$	$5.31\cdot10^{-07}$
$1\cdot10^{-02}$	$4.10\cdot10^{-05}$	$2.09\cdot10^{-07}$	$5.89\cdot10^{-04}$	$4.72\cdot10^{-04}$
$1\cdot10^{-01}$	$1.39\cdot10^{-02}$	$9.00\cdot10^{-05}$	$1.30\cdot10^{-01}$	$1.18\cdot10^{-01}$

Table 6. Typical relative error values in Bishop's stress $\boldsymbol{\sigma}^*$, degree of saturation S_r, mechanical hardening parameter p_0' and wetting retention hardening parameter s_{10}^* for

a single elasto-plastic isotropic loading step at constant suction for Runge-Kutta-Dormand-Prince with substepping (RKDP5) considering *STOL*=1.

$\Delta\varepsilon_v$	Error in $\boldsymbol{\sigma}^*$	Error in S_r	Error in p_0'	Error in s_{10}^*
$1{\cdot}10^{-06}$	$< 1.0{\cdot}10^{-15}$	$< 1.0{\cdot}10^{-15}$	$< 1.0{\cdot}10^{-15}$	$< 1.0{\cdot}10^{-15}$
$1{\cdot}10^{-05}$	$< 1.0{\cdot}10^{-15}$	$< 1.0{\cdot}10^{-15}$	$< 1.0{\cdot}10^{-15}$	$< 1.0{\cdot}10^{-15}$
$1{\cdot}10^{-04}$	$< 1.0{\cdot}10^{-15}$	$< 1.0{\cdot}10^{-15}$	$< 1.0{\cdot}10^{-15}$	$< 1.0{\cdot}10^{-15}$
$1{\cdot}10^{-03}$	$< 1.0{\cdot}10^{-15}$	$< 1.0{\cdot}10^{-15}$	$< 1.0{\cdot}10^{-15}$	$< 1.0{\cdot}10^{-15}$
$1{\cdot}10^{-02}$	$1.02{\cdot}10^{-11}$	$< 1.0{\cdot}10^{-15}$	$2.39{\cdot}10^{-09}$	$1.91{\cdot}10^{-09}$
$1{\cdot}10^{-01}$	$6.94{\cdot}10^{-06}$	$5.31{\cdot}10^{-12}$	$1.33{\cdot}10^{-03}$	$1.06{\cdot}10^{-03}$

The respective gradients of each best-fitted straight line plotted in both figures match the expected order of accuracy of the method, suggesting that both substepping schemes work correctly at a single step/substep level. In particular, for both tests, approximate gradients of 6 are obtained when best-fitting a straight line through the computed error values in $\boldsymbol{\sigma}^*$, S_r, p_0' and s_{10}^* corresponding to the RKDP5 method and approximate gradients of 3 are obtained when best-fitting a straight line through the computed error values in $\boldsymbol{\sigma}^*$, S_r, p_0' and s_{10}^* corresponding to the ME2 method. Note that, for completeness, Figures 7 and 8 also include the best-fitted lines for the computed error values for the single-step first order forward Euler (gradient 2) and single-step fourth order Runge-Kutta-Dormand-Prince (gradient 5) integration schemes, in addition to the error results for ME2 and RKDP5.

The results in Figures 7 and 8 show that the specific values of the local relative error incurred in each variable considered during the numerical integration, differ in each numerical test considered. In particular, the variation of the position of each best-fitted line (i.e. intercept) differs in each test and for each variable considered. This behaviour justifies the decision of treating separately the local error from mechanical (i.e. $\boldsymbol{\sigma}^*$ and p_0') and water retention (i.e. S_r and s_{10}^*) responses.

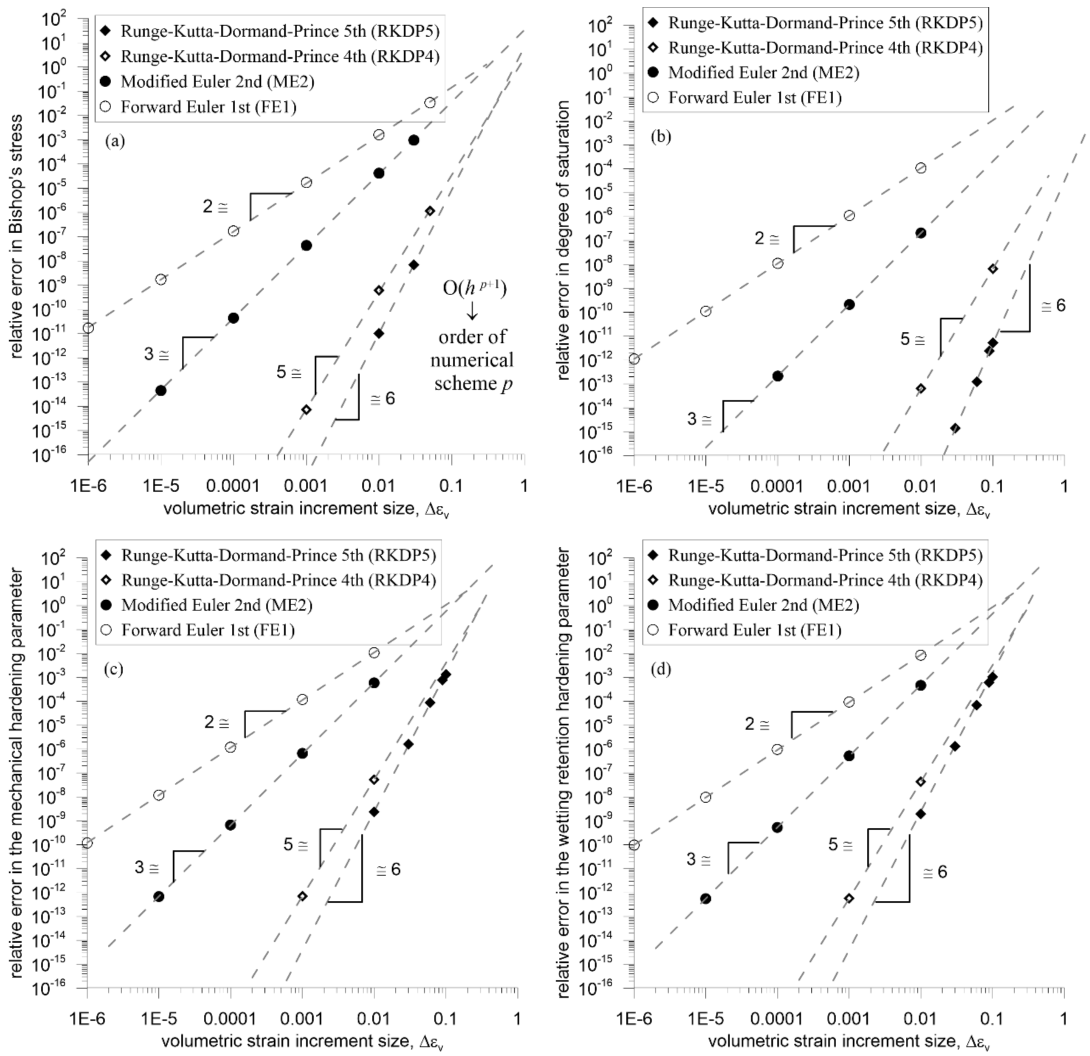

Figure 7. Relative error for single-step explicit integration schemes against volumetric strain increment size for a single elasto-plastic isotropic strain increment at constant suction: (a) Bishop's stress $\boldsymbol{\sigma}^{*}$; (b) degree of saturation S_r; (c) mechanical hardening parameter p_0'; (d) water retention hardening parameter s_{10}^{*}.

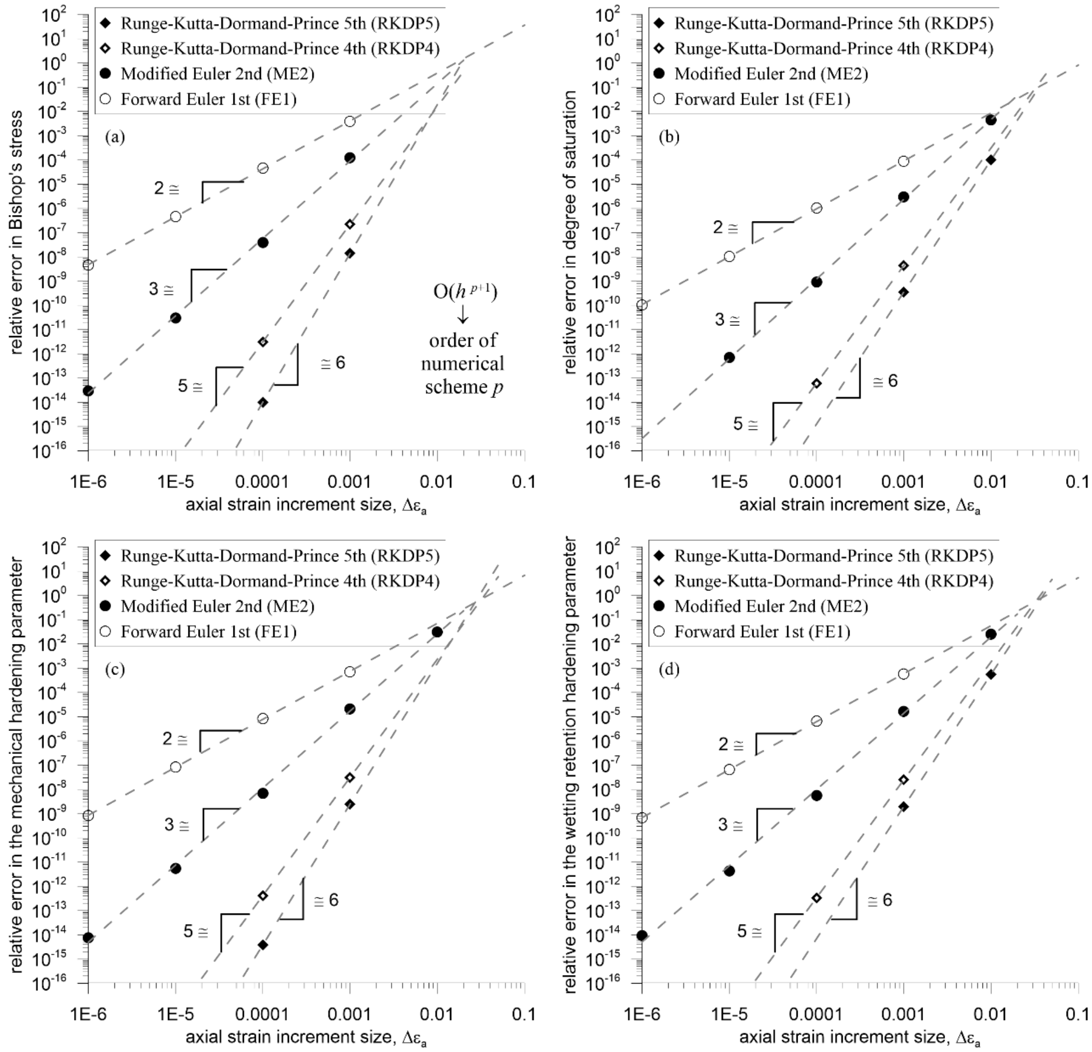

Figure 8. Relative error for single-step explicit integration schemes against axial strain increment size for a single elasto-plastic axial strain increment (at constant radial strain) under wetting: (a) Bishop's stress $\boldsymbol{\sigma}^{*}$; (b) degree of saturation S_r; (c) mechanical hardening parameter p_0'; (d) water retention hardening parameter s_{10}^{*}.

5.2. Substepping analysis: cumulative relative error

Once a substepping integration scheme has been verified at a single step level, the verification process should study the numerical performance over several substeps. In this context, Lloret-Cabot et al. (2016) propose to study the behaviour of the cumulative relative error E incurred in an integration scheme when the substepping is active. Assuming no cancellation, the addition of each amount of relative error e incurred in each substep corresponds to the cumulative relative error E. Lloret-Cabot et al. (2016) show that $e \cong ch^{p+1}$ (where h is the substep size, p is the order of the integration scheme and c is simply a constant that fixes the position of an error line for a single step/substep in the ln$e$:ln$h$ plane) and that, for n equal-sized substeps of size h, $E \cong nch^{p+1} = Hch^{p}$ (where H is the size of the total increment integrated i.e. H=hn). This means that the final cumulative error (incurred during the integration of a given total increment H) approximately lies on a straight line when plotted against the substep size h in a log-log scale, having gradient 2 for the ME2 and 5 for RKDP5 with substepping schemes. Similarly to the error lines for a single step/substep, the intercept of a cumulative error line is Hc (as $E \cong Hch^{p}$) and, hence, the distance between the best-fitted straight line for the single-step error and a cumulative error line for an increment involving many substeps can be checked at a particular step/substep size h (Lloret-Cabot et al. 2016).

The numerical integration of Tests A and B is performed again using the ME2 and RKDP5 schemes with substepping but now imposing values of *STOL* small enough to activate the substepping. In the analyses presented next, the maximum number of substeps is limited to 10^{+06} and the values for *STOL* vary from 1 to 10^{-08}.

The study of the numerical performance of each integration scheme is in two parts. An investigation on how the errors are accumulated over the substeps integrated is presented first, to check that the computed cumulative error is consistent with that of the numerical method used. The performance maps proposed in Lloret-Cabot et al. (2016) are presented in the second part of the analysis to check that the substepping integration performs correctly. Without loss of generalisation, the first part of the analysis is carried out only for Test A. The study of the performance maps, on the other hand, is carried out for both numerical tests.

The different values of *STOL* considered (from 1 to 10^{-08}) together with the accumulated contributions of relative error at each substep are illustrated in Figures 9 and 10 for the ME2 and RKDP5 schemes with substepping, respectively. Tables 7 and 8 present typical values of cumulative relative error for ME2 and RKDP5 substepping schemes, respectively, during the numerical integration of a volumetric strain increment of 0.1 for *STOL* = 10^{-02}, 10^{-04}, 10^{-06} and 10^{-08} (Test A). In the tables, the total number of substeps required in the algorithm is indicated by TS whereas the total number of failed substeps (substeps requiring a further subdivision in size) is indicated by TF. No drift correction iterations were necessary in Test A.

Table 7. Typical cumulative relative error values in Bishop's stress $\boldsymbol{\sigma}^*$, degree of saturation S_r, mechanical hardening parameter p_0' and wetting retention hardening parameter s_{10}^* for an elasto-plastic isotropic strain increment of $\Delta\varepsilon_v = 0.1$ at constant suction for the modified Euler with substepping (ME2) considering different values of *STOL*.

STOL	Error in $\boldsymbol{\sigma}^*$	Error in S_r	Error in p_0'	Error in s_{10}^*	TS	TF
$1\cdot10^{-02}$	$2.96\cdot10^{-04}$	$1.44\cdot10^{-06}$	$4.45\cdot10^{-03}$	$3.57\cdot10^{-03}$	11	2
$1\cdot10^{-04}$	$2.79\cdot10^{-06}$	$1.32\cdot10^{-08}$	$4.45\cdot10^{-05}$	$3.56\cdot10^{-05}$	114	3
$1\cdot10^{-06}$	$2.78\cdot10^{-08}$	$1.31\cdot10^{-10}$	$4.46\cdot10^{-07}$	$3.57\cdot10^{-07}$	1141	4
$1\cdot10^{-08}$	$2.78\cdot10^{-10}$	$1.31\cdot10^{-12}$	$4.46\cdot10^{-09}$	$3.57\cdot10^{-09}$	11416	5

Table 8. Typical cumulative relative error values in Bishop's stress $\boldsymbol{\sigma}^*$, degree of saturation S_r, mechanical hardening parameter p_0' and wetting retention hardening parameter s_{10}^* for an elasto-plastic isotropic strain increment of $\Delta\varepsilon_v = 0.1$ at constant suction for the Runge-Kutta-Dormand-Prince with substepping (RKDP5) considering different values of *STOL*.

STOL	Error in $\boldsymbol{\sigma}^*$	Error in S_r	Error in p_0'	Error in s_{10}^*	TS	TF
$1\cdot10^{-02}$	$6.94\cdot10^{-06}$	$5.30\cdot10^{-12}$	$1.33\cdot10^{-03}$	$1.06\cdot10^{-03}$	1	0
$1\cdot10^{-04}$	$3.95\cdot10^{-07}$	$1.22\cdot10^{-13}$	$8.87\cdot10^{-05}$	$7.10\cdot10^{-05}$	2	2
$1\cdot10^{-06}$	$1.07\cdot10^{-09}$	$1.24\cdot10^{-15}$	$2.72\cdot10^{-07}$	$2.17\cdot10^{-07}$	6	2
$1\cdot10^{-08}$	$8.38\cdot10^{-12}$	$1.24\cdot10^{-15}$	$2.16\cdot10^{-09}$	$1.73\cdot10^{-09}$	16	2

The form of plotting the results shown in Figures 9 and 10 is particularly convenient to study how the cumulative relative error increases as the integration progresses (indicated by a series of data points forming a near vertical path in the figure) for various values of *STOL*. During a typical substepping integration of a prescribed volumetric strain increment $\Delta\varepsilon_v$ with n substeps, the relative error incurred in each of these substeps (all fulfilling the imposed *STOL*) accumulates over the substeps to give a value of the cumulative relative error (Lloret-Cabot et al., 2016). Figures 9 and 10 demonstrate that, indeed, the final values of cumulative relative error once the entire $\Delta\varepsilon_v$ has been integrated approximately lie on a straight line of gradient two for the ME2 with substepping and five for the RKDP5 with substepping (see dashed lines). This behaviour is true for all values of *STOL* used (Figures 9 and 10). The vertical distance (measured upwards) from the best-fitted straight line for the single substep relative error (indicated by a thicker dark line) and one of these cumulative relative error lines (at a particular total increment size $\Delta\varepsilon_v$ and substep size $\delta\varepsilon_v$) corresponds to $1/n$ where n is the number of substeps (Lloret-Cabot et al., 2016). This error response is illustrated in Figure 9 for three different sizes of volumetric strain increment (i.e. 0.001, 0.01 or 0.1), when using the ME2 with substepping and a value of *STOL*=10^{-08}. A total number of 118 substeps are needed to integrate the volumetric strain increment size of 0.001, 1185 for 0.01 and 11416 for 0.1. This response is less apparent when using the RKDP5 scheme because of the small number of substeps typically required in this higher order method (Figure 10).

During the numerical integration of each $\Delta\varepsilon_v$ considered, the actual substep size being integrated is quite regular in the two substepping schemes considered as reflected by the approximately vertical paths traced by the cumulative error (Figures 9 and 10).

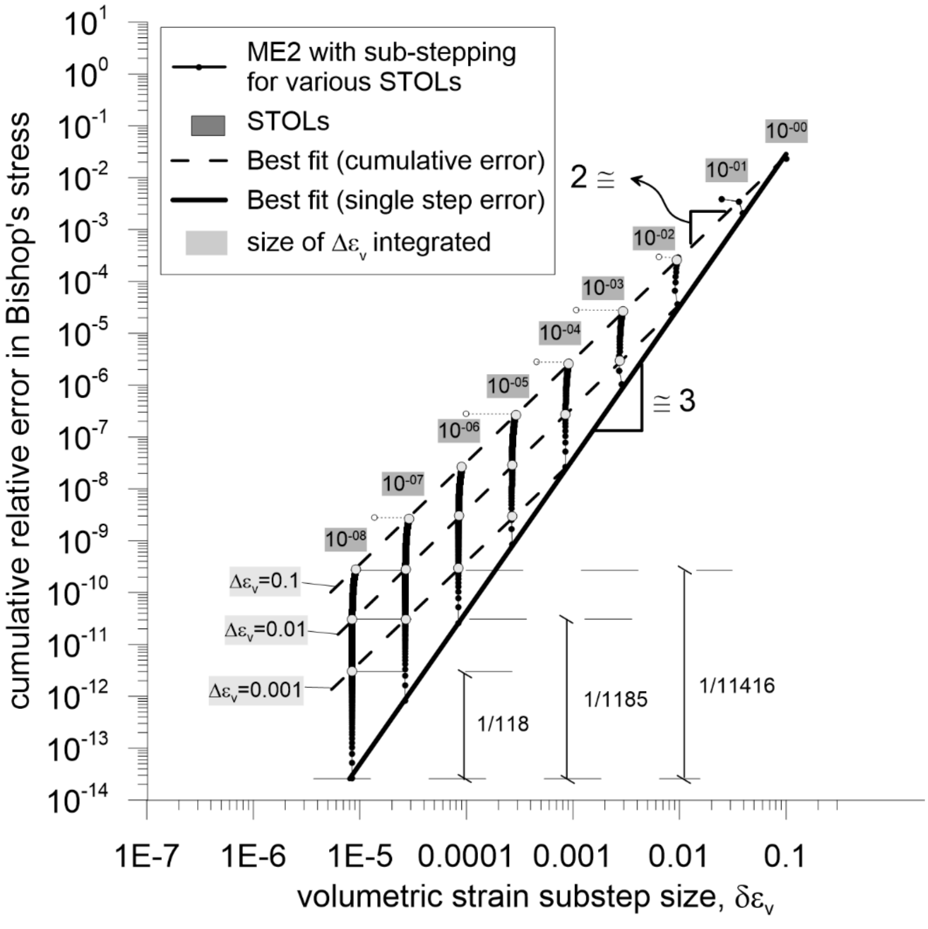

Figure 9. Cumulative relative error behaviour in Bishop's stresses for the modified Euler with substepping (ME2) integration scheme with different values of *STOL* against strain increment size for an elasto-plastic isotropic loading increment.

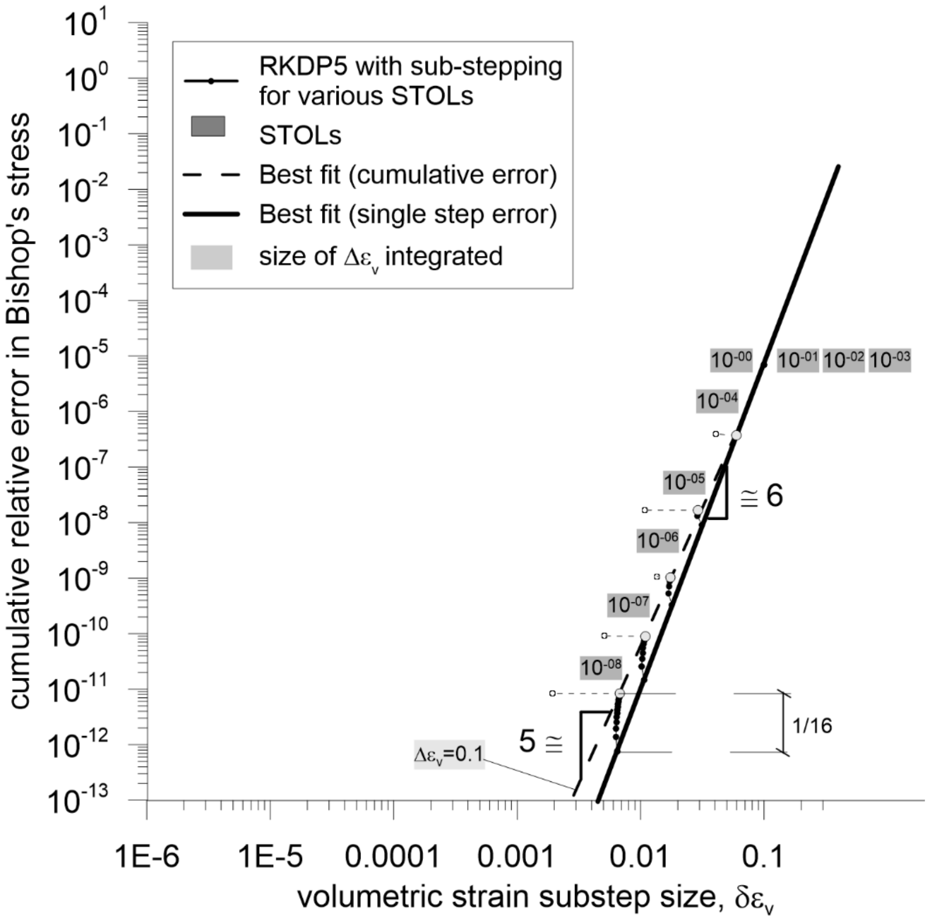

Figure 10. Cumulative relative error behaviour in Bishop's stresses for the Runge-Kutta-Dormand-Prince with substepping (RKDP5) integration scheme with different values of *STOL* against strain increment size for an elasto-plastic isotropic loading increment.

Figure 11 shows the cumulative relative error (i.e. the accumulated relative error incurred over the number of substeps required to integrate a given increment of volumetric strain) for Bishop's stresses incurred in Test A plotted against *STOL* for each integrated size of volumetric strain increment $\Delta\varepsilon_v$. Figure 12 plots the same cumulative relative error plotted against the number of substeps required for the integration of the entire strain increment. In these figures, part a) presents the results for the ME2 with substepping and part b) their RKDP5 substepping counterparts.

Inspection of Figure11 shows how the influence of *STOL* in the relative error incurred in an individual substep $\delta\varepsilon_v$ affects the cumulative relative error incurred in the integration of the entire $\Delta\varepsilon_v$. As expected, a reduction in the values of *STOL* leads to a reduction in the relative error incurred in each individual substep of the computations which, in turn, reduces the cumulative relative error. However, this reduction of the cumulative relative error with decreasing *STOL* is not apparent for small sizes of volumetric strain increment unless *STOL* is less than a critical size (Figure 11). Similarly to what is observed in saturated soils (Lloret-Cabot et al., 2016), this is because for small increment sizes, even without substepping the difference between the two solutions of different order within the substepping scheme tends to be very small and, if it is less than the *STOL* considered, the substepping strategy is not activated. For example, for a volumetric strain increment size of 10^{-02}, values of *STOL* smaller than 10^{-02} are required to activate the substepping strategy with the ME2 scheme (Point Y in Figure 11a). The RKDP5 with substepping, on the other hand, needs values of *STOL* smaller than 10^{-06} to activate substepping for a volumetric strain increment size of 10^{-2} (Point Y in Figure 11b). Figure 11a shows that for a volumetric strain increment size of 10^{-02}, 1186 substeps are required in the ME2 substepping scheme (with $STOL = 10^{-08}$) to reach a cumulative relative error of about 10^{-10}. In contrast, the RKDP5 substepping scheme requires only 2 substeps to reach a similar (even substantially smaller) value of the cumulative relative error (see Figure 11b).

As discussed earlier, the second order accurate modified Euler with substepping uses $r \cong 0.9(STOL/REL_n)^{1/2}$ and the fifth order accurate Runge-Kutta-Dormand-Prince with substepping uses $r \cong 0.9(STOL/REL_n)^{1/5}$. This means that the variation of the cumulative relative error with the number of substeps should follow, approximately, straight lines of gradient -2 for the ME2 integration scheme and, similarly, approximately straight lines of gradient -5 for the RKDP5 integration scheme as correctly illustrated in Figure 12.

The plots presented in Figure 11 and 12 correspond to the performance maps proposed in Lloret-Cabot et al. (2016) for saturated soils and its application is demonstrated here for unsaturated soils. The results obtained confirm that this specific form of plotting the computational outcomes from a substepping integration scheme is a powerful verification tool.

Similar error responses to those just discussed for Figure 12 are also observed in Figure 13 (Test B) for $\boldsymbol{\sigma}^*$, S_r, p_0' and s_{10}^* when using the ME2 substepping integration scheme. Even in the case of not using an analytical solution to compute the relative error, the error behaviour observed is consistent with that discussed when analytical solutions were available.

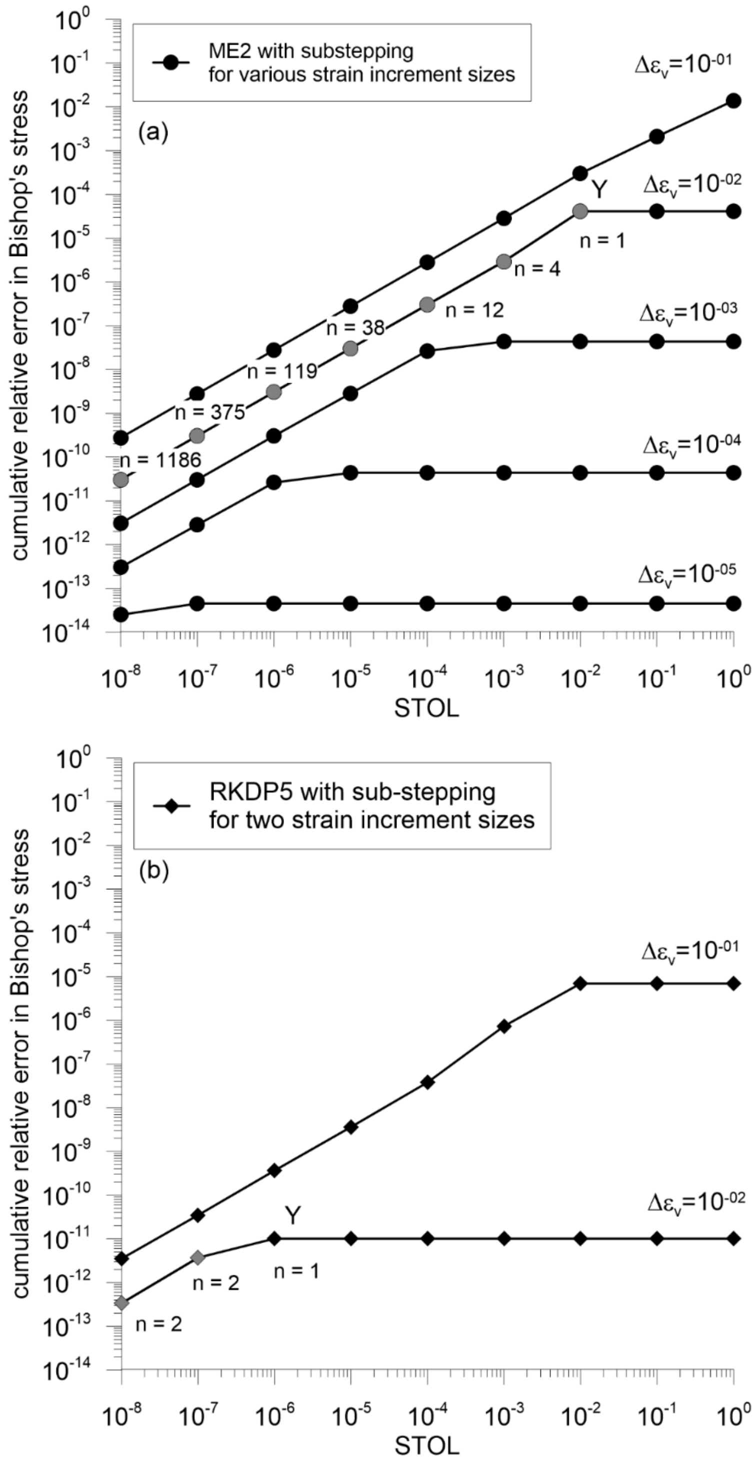

Figure 11. Cumulative relative error behaviour against *STOL* for an elasto-plastic isotropic strain increment at constant suction: (a) Modified Euler with substepping scheme (ME2); (b) Runge-Kutta-Dormand-Prince with substepping scheme (RKDP5).

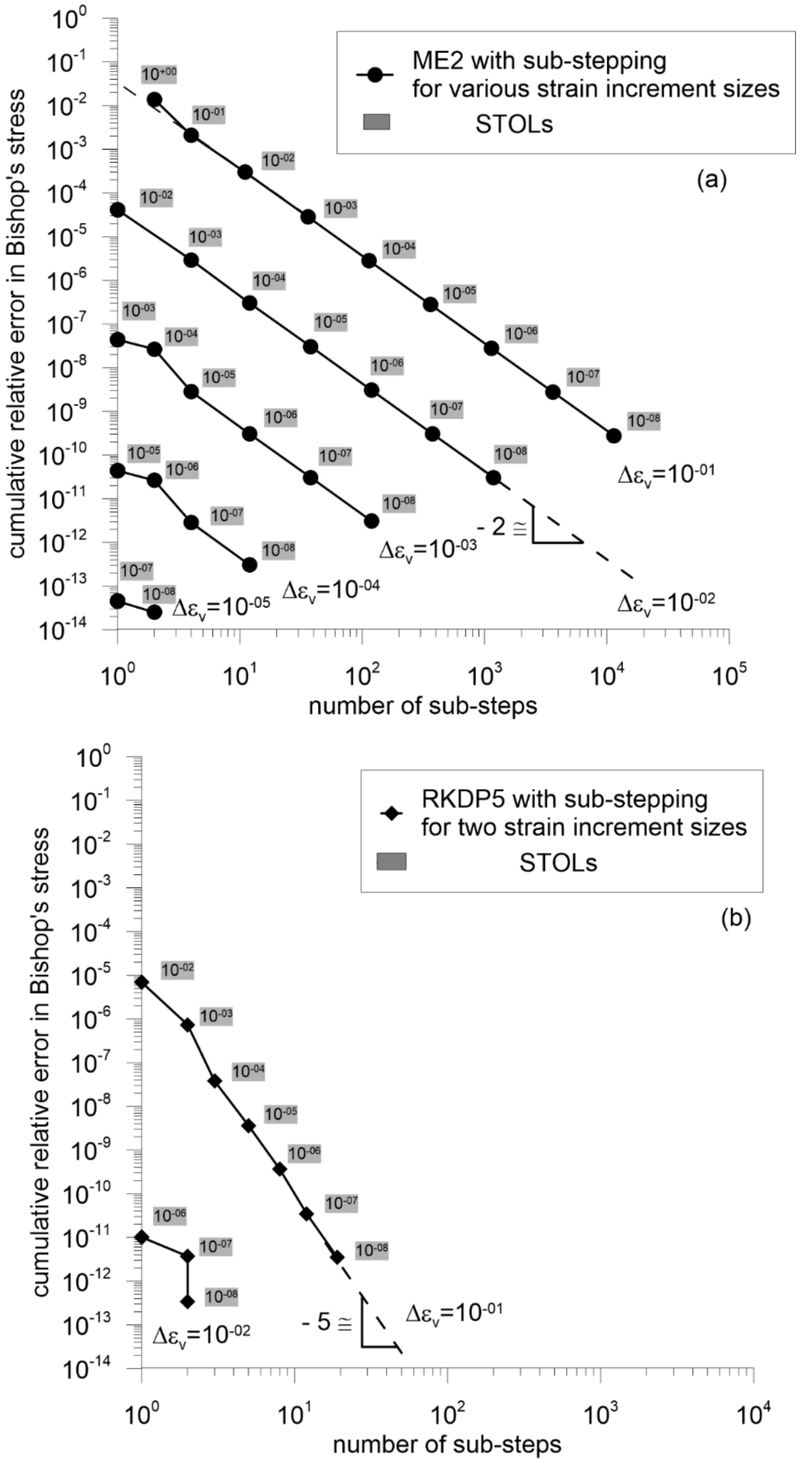

Figure 12. Cumulative relative error behaviour against number of substeps for an elasto-plastic isotropic strain increment at constant suction: (a) Modified Euler with substepping scheme (ME2); (b) Runge-Kutta-Dormand-Prince with substepping scheme (RKDP5).

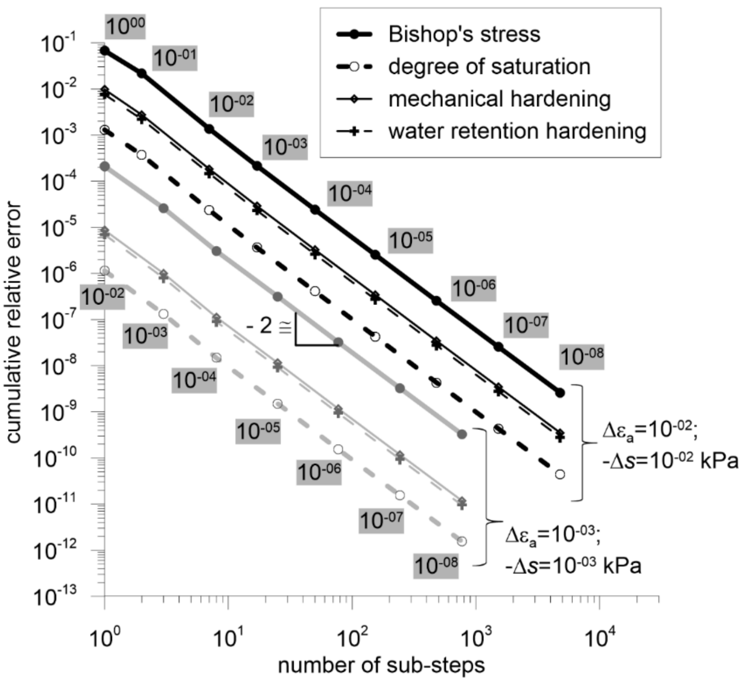

Figure 13. Cumulative relative error behaviour against number of substeps for an elasto-plastic axial strain increment (at constant radial strain) under wetting using the modified Euler with substepping scheme (ME2).

5.3. Computational cost and efficiency

The simplicity of the numerical examples discussed above implies a very small CPU time and, therefore, it is reasonable to assess the computational cost associated with each example as proportional to the number of evaluations of the constitutive relations that the substepping integration scheme employs to solve the problem (Sloan et al., 2001). Equivalently to Lloret-Cabot et al. (2016), two evaluations of the constitutive relations are required in the ME with substepping scheme and six are needed in the RKDP substepping scheme. Additionally, the computational cost associated with any rejected step as well as the computational cost associated with the number of iterations used by the drift correction subroutine are also accounted for.

Figure 14 shows the computational cost as a function of *STOL* (i.e. *STOL*= 10^{-02}, 10^{-04}, 10^{-06} and 10^{-08}), and the input increment size for the three numerical tests considered earlier. Plots on the left correspond to the ME substepping scheme and plots on the right show the approximations for the RKDP substepping scheme. A similar pattern to that found by Lloret-Cabot et al. (2016) when using the MCC model is also observed here for the GCM. In general, from the two integration schemes investigated, the ME substepping scheme requires a larger number of evaluations of the constitutive relations (i.e. higher computational cost) to satisfy the value of *STOL* when the sizes of the input increment $\Delta\varepsilon_v$, $\Delta\varepsilon_a$, or Δs are large (and this observation is more pronounced when the values of *STOL* are more restrictive). In contrast, the RKDP substepping scheme is more expensive for the smaller increment sizes. For intermediate increment sizes, the optimal computational efficiency depends on the level of accuracy specified (RKDP substepping scheme is most efficient for stringent tolerances whereas ME substepping scheme is best for looser values of *STOL*).

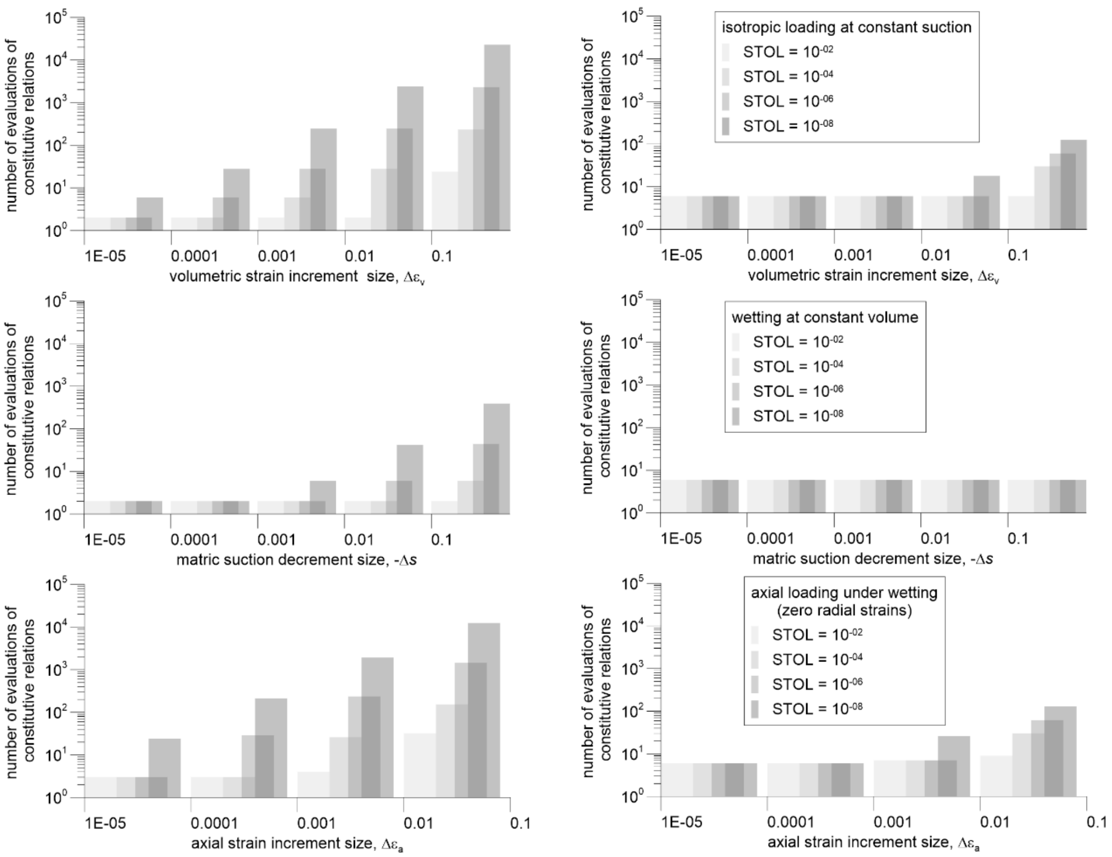

Figure 14. Computational cost for different STOL values against input increment sizes: (left) modified Euler substepping scheme; (right) Runge-Kutta-Dormand-Prince substepping scheme.

6. CONCLUSIONS

The complete formulation of the incremental constitutive relations of the Glasgow Coupled Model (GCM) has been presented for all possible elastic and elasto-plastic responses of the model, including transitions between saturated and unsaturated conditions. The formulation is expressed in terms of the increments of strain and increments of suction (i.e. strain-driven formulation) so that it is suitable for implementation into a finite element program, as it properly defines an initial value problem (IVP) when the initial stress state and the increments of strain and suction are known.

A rigorous algorithm capable of identifying unambiguously which is the model response activated by a trial stress path has been developed after a small reformulation of the GCM that included the derivation of a useful closed-form expression for the mechanical yield curve in terms of degree of saturation. The correct identification of the intersection point, when a trial stress path moves from elastic to elasto-plastic behaviour, is achieved by using the Pegasus algorithm, widely used for solving the equivalent problem in explicit formulations for saturated soil models. The same strategy is applied to find the correct stress point at saturation and desaturation. A drift correction subroutine has been also presented to correct any potential deviation of the stress point at the end of each integrated elasto-plastic step/substep.

Two explicit substepping formulations to integrate numerically the IVP defined by the initial state and the incremental relations of the GCM have been then presented, extending to unsaturated conditions the well-known explicit substepping integration schemes with automatic error control for saturated soils. These two substepping schemes presented correspond to the second order accurate modified Euler with substepping and the fifth order accurate Runge-Kutta-Dormand-Prince with substepping.

In contrast to existing substepping formulations with automatic error control for saturated soils, which account only for the relative error associated with the integration of the mechanical part of the problem (i.e. stresses and mechanical hardening parameter), the extended substepping version with automatic error control presented in this paper accounts for the relative error incurred during the numerical integration of both the mechanical (stresses and mechanical hardening parameter) and water retention (degree of saturation and water retention hardening parameter) components of the problem. This is essential when applying substepping schemes to solve problems involving unsaturated soils, as this is what ensures an accurate and efficient integration.

The correctness of the two substepping schemes presented is checked by investigating how the error over an individual step/substep and the cumulative error over multiple substeps propagate during the integration of two simple numerical tests, involving an isotropic straining at constant suction and a combined axial straining under wetting. The behaviour of the relative error observed when adopting a single-step integration in solving each of these tests is different for the mechanical and the water retention components of the problem, which confirms the importance of accounting separately for the different sources of error. The computational performance of the two substepping schemes is then checked by ensuring that the influence of the internal substepping tolerance *STOL* on the accuracy and the number of substeps used is as expected. The results obtained extend to unsaturated conditions the conclusions observed for saturated soils (Lloret-Cabot et al., 2016), confirming that the substepping methods proposed are capable of controlling the cumulative error (i.e. they satisfy the error tolerance *STOL* for all the cases considered).

Finally, this investigation confirms that the importance of updating rigorously the specific volume in Cam Clay family models for saturated soils in substepping integration schemes extends also to the rigorous update of the degree of saturation in substepping integration schemes for critical state models for unsaturated soils.

7. ACKNOWLEDGEMENTS

This research has benefitted from the Marie-Skłodowska Curie project "*COUPLED*" funded from the H2020 programme of the EC (MSCA-IF-2015-706712). Support from the project "*TERRE*" (ETN-GA-2015-675762) of the EU is also acknowledged.

8. APPENDICES

8.1 Appendix A

The Glasgow Coupled Model (GCM) predicts that isotropic stress states at the intersection of f_M and f_{WR} yield curves fall on unique unsaturated isotropic normal compression planar surfaces for v (in v: $\ln p^*$: $\ln s^*$ space) and also for S_r (in S_r: $\ln p^*$

$:\ln s^*$ space). The forms of these two planar surfaces are (see also Lloret-Cabot et al. 2017):

$$v = \mathrm{N}^* - \lambda^* \ln p_0^* + k_1^* \ln s_1^* \tag{A1}$$

$$S_r = \Omega^* - \lambda_s^* \ln s_1^* + k_2^* \ln p_0^* \tag{A2}$$

where N^* and Ω^* are their respective intercepts. The expressions of gradients λ^*, k_1^*, λ_s^* and k_2^* are a combination of the soil parameters of the model (assuming $\mathrm{d}S_r^e = 0$):

$$\lambda^* = \frac{\lambda - k_1 k_2 \kappa}{1 - k_1 k_2} \tag{A3}$$

$$k_1^* = k_1 \frac{\lambda - \kappa}{1 - k_1 k_2} \tag{A4}$$

$$\lambda_s^* = \frac{\lambda_s}{1 - k_1 k_2} \tag{A5}$$

$$k_2^* = k_2 \frac{\lambda_s}{1 - k_1 k_2} \tag{A6}$$

Assuming $\kappa_s = 0$ (the gradient of elastic scanning curves in the S_r:lns^* plane as defined in Wheeler et al., 2003), Lloret-Cabot et al. (2017) derives the following relationship between intercepts N, N^* and Ω^*:

$$\Omega^* = 1 - \frac{\left(\mathrm{N}^* - \mathrm{N}\right)\lambda_s}{k_1\left(\lambda - \kappa\right)} \tag{A7}$$

Combining the above equations with the elastic relations of the GCM, it is possible to find the following expressions for v for any general stress state (Lloret-Cabot et al., 2017):

$$v = \mathrm{N}^* - \lambda^* \ln p_0^* + k_1^* \ln s_1^* + \kappa \ln\left(\frac{p_0^*}{p^*}\right) \tag{A8}$$

Equation A8 can be used to calculate initial value of v when initial values of p^*, p_0^* and s_1^* are known, together with the model parameters. Given that $\mathrm{d}S_r^e = 0$, the initial value of S_r can be also calculated from Equation A2 (Lloret-Cabot et al., 2017).

8.2 Appendix B

A more formalised description of the sequence of the steps followed by the algorithm to determine which is the active response of the GCM is presented here for the most general case of a stress point starting inside the three yield curves of the model and potentially activating any of the six possible model responses. Any other case (i.e. stress point starting on one or two yield curves) is a particular case of this one.

(A) Compute *trial 1* assuming purely elastic behaviour.

- If *trial 1* is inside f_M, f_{DR} and f_{WR} then, elastic update from i to i+1 and *return*.
- If *trial 1* is outside f_M, outside f_R or outside both, yielding has occurred (note that f_R is either f_{DR} or f_{WR}). Hence:
  - If *trial 1* is outside only one yield curve (f_M or f_R).
    - Find the portion α of Δ**ε** and Δs, that moves the stress point to the intersection with f_M, i_{M1}, (or with f_R, i_{R1}). Note that α = 0 means that the stress point was already on f_M (or f_R).
    - Update elastic from i to i_{M1} (or i_{R1}).
    - Move to *trial 2* with the portion not yet integrated of Δ**ε** and Δs given by (1-α). At this stage, the stress point is on f_M (or on f_R).
  - If *trial 1* is outside two yield curves (f_M and f_R).
    - Find intersection with f_M, α_1.
    - Find intersection with f_R, α_2.
  - If $\alpha_1 < \alpha_2$ then f_M is reached first.
    - Update elastic from i to i_{M1} using α_1.
    - Move to *trial 2* with (1-α_1). The stress point is on f_M
  - If $\alpha_2 \leq \alpha_1$then f_R is reached first.
    - Elastic update from i to i_{R1} using α_2 (note that if $\alpha_1 = \alpha_2$, then i_{R1}=i_{M1} and, hence, $\alpha_1 = \alpha_2$ =0 i.e. stress point is on both f_M and f_R)
    - Move to *trial 2* with (1-α_2). The stress point is on f_R (if $\alpha_2 < \alpha_1$) or on both f_R and f_M (if $\alpha_2 = \alpha_1$).

(B) At this stage, there are three possible ways to compute *trial 2* depending on whether the stress point is on f_M (point i_{M1}, case B.1) on f_R (point i_{R1}, case B.2) or on both (point i_Y, case B.3).

(B.1) If the stress point is only on f_M (point i_{M1}) then,

Compute *trial 2* assuming yielding on f_M, but not on f_R (using the portion not yet integrated of $\Delta\boldsymbol{\varepsilon}$ and Δs i.e. (1-α) if *trial 1* crosses only one yield curve or (1-α_1) if *trial 1* crosses two yield curves).

If *trial 2* is inside f_R, then yielding on f_M (but not on f_R) has occurred.

Update stress point from i_{M1} to i_{M1}+1 assuming yielding on f_M alone (using 1-α or 1-α_1) and *return*.

If *trial 2* is outside f_R, then *trial 2* crosses f_R at point i_Y, on both f_M and f_R.

Find intersection with f_R $i_R = i_Y$, β. Note that β = 0 means that the stress point was already on f_R.

Update stress point from i_{M1} to i_R assuming yielding on f_M alone (using β) and move to *trial 3*.

At this stage, the stress point is on f_M and f_R (point i_Y). There are only two possible model responses here: yielding on only f_R or simultaneous yielding on f_M and f_R. Yielding on only f_M is not possible because, if that was the case, *trial 2* would had fallen inside f_R when assuming yielding on only f_M and, in fact, the algorithm is at this point because *trial 2* fell outside f_R.

Compute *trial 3* assuming yielding on f_R (but not on f_M) with (1-β).

If *trial 3* is inside f_M, then update the stress point from i_Y to i_Y+1 assuming yielding on f_R alone (using 1-β) and *return*.

Otherwise, update the stress point from i_Y to i_Y+1 assuming simultaneous yielding on f_M and f_R (using 1-β) and *return*.

(B.2) If the stress point is on f_R (point i_{R1}) then,

Compute *trial 2* assuming yielding on f_R (but not on f_M) using the portion not yet integrated of $\Delta\boldsymbol{\varepsilon}$ and Δs i.e. (1-α) or (1-α_2).

If *trial 2* is inside f_M, then yielding on f_R (but not on f_M) has occurred

Update stress point from i_{R1} to i_{R1}+1 assuming yielding on f_R alone (using 1-α or 1-α_2) and *return*.

If *trial 2* is outside f_M, then *trial 2* crosses f_M at point i_Y, on both f_M and f_R.

Find intersection with f_M $i_M = i_Y$, β.

Update stress point from i_R to i_M assuming yielding on f_R alone (using β) and move to *trial 3*.

At this stage, the stress point is on f_M and f_R (point i_Y). There are only two possible model responses here: yielding on only f_M or simultaneous yielding on f_M and f_R. Note that yielding on only f_R is not possible because, if that was the case, *trial 2* would had fallen inside f_M when assuming yielding on only f_R and, in fact, fell outside f_M.

Compute *trial 3* assuming yielding on f_M (but not on f_R) with (1-β).

If *trial 3* is inside f_R, then update the stress point from i_Y to i_Y+1 assuming yielding on f_M alone (using 1-β) and *return*.

Otherwise, update the stress point from i_Y to i_Y+1 assuming simultaneous yielding on f_M and f_R (using 1-β) and *return*.

(B.3) If the stress point is on f_M and f_R (point i_Y). There are three possible model responses here: yielding on only f_R, yielding on only f_M or simultaneous yielding on f_M and f_R. Therefore, the algorithm may need to compute a maximum of two trials to ensure the correct model response.

Compute *trial 2* assuming yielding on f_R, (but not on f_M) using the portion not yet integrated of $\Delta\boldsymbol{\varepsilon}$ and Δs i.e. (1-α) or (1-α_2).

If *trial 2* is inside f_M, then yielding on f_R (but not on f_M) has occurred.

Update from i_Y to i_Y+1 assuming yielding on f_R alone (using 1-α or 1-α_2) and *return*.

Otherwise, move to *trial 3*.

Compute *trial 3* assuming yielding on f_M (but not on f_R) using the portion not yet integrated of $\Delta\boldsymbol{\varepsilon}$ and Δs i.e. (1-α) or (1-α_2).

If *trial 3* is inside f_R, then update the stress point from i_Y to i_Y+1 assuming yielding on f_M alone and *return*.

Otherwise, update the stress point from i_Y to i_Y+1 assuming simultaneous yielding on f_M and f_R and *return*.

Note that step (B.3) can be accommodated in steps (B.1) or (B.2), but, for clarification, it has been kept as a separate case.

8.3 Appendix C

Given the increments of $\Delta\boldsymbol{\varepsilon}$ and Δs, the stress state can move from elastic to elasto-plastic. In the context of the GCM, this means that a *trial* intersects at least one yield curve and that an intersection point needs to be found. The proposed integration schemes solve all intersections using the Pegasus algorithm illustrated in Figure C1 (Dowell and Jarratt, 1972). Two conditions are necessary for a *trial* to cross a generic yield curve f_A. The first one is that the stress point at *i* is not already lying on f_A (indicated in Figure C1 as $^0f_A < -FTOL$). The second one is that the evaluation of the yield curve at the *trial* is larger than *FTOL* (indicated by $^1f_A > FTOL$ in Figure C1). If both of these conditions are true, the Pegasus algorithm finds the scalar α that defines the portion of $\Delta\boldsymbol{\varepsilon}$ and Δs that moves the current stress point to f_A (indicated as *i* in Figure C1). A value of $\alpha = 0$ indicates that the initial stress point is already on f_A (i.e. $|f_A| \leq FTOL$) and the update of the stress point is elasto-plastic. A value $\alpha = 1$ indicates that the final stress point (once the full size of $\Delta\boldsymbol{\varepsilon}$ and Δs has been updated) ends up exactly on f_A so that no intersection occurs. These two extreme cases explain why the possible values of the scalar α range between 0 and 1.

if $\left({}^{1}f_{\mathrm{A}} > FTOL\right)$ ***then*** !$^{1}f_{\mathrm{A}}$ corresponds to $^{trial}f_{\mathrm{A}}$

if $\left({}^{0}f_{\mathrm{A}} < -FTOL\right)$ ***then*** !$^{0}f_{\mathrm{A}}$ corresponds to $^{i}f_{\mathrm{A}}$

$\alpha_0 = 0$

$\alpha_1 = 1$

GO TO **1**

endif

! stress point on f_{A} at i

$\alpha = 0$

GO TO **3**

1 *continue*

! Find the elastic portion α of ($\Delta\boldsymbol{\varepsilon}$, Δs) that moves the stress point to $^{0}f_{\mathrm{A}}$

do **2** $n = 1$, maxit ! maxit is the maximum number of iterations

$\alpha = \alpha_1 - (\alpha_1 - \alpha_0)\,{}^{1}f_{\mathrm{A}} \big/ \left({}^{1}f_{\mathrm{A}} - {}^{0}f_{\mathrm{A}}\right)$

$^{t}\Delta\boldsymbol{\varepsilon} = \alpha\Delta\boldsymbol{\varepsilon}$ and $^{t}\Delta s = \alpha\Delta s$

update with $^{t}\Delta\boldsymbol{\varepsilon}$ *and* $^{t}\Delta s$

f_A ! Evaluation of f_{A} at the updated point

if $\left(\left|f_{\mathrm{A}}\right| \le FTOL\right)$ ***then***

GO TO **3**

endif

if $\left({}^{0}f_{\mathrm{A}} \cdot \ f_{\mathrm{A}} > 0\right)$ ***then***

$^{1}f_{\mathrm{A}} = {}^{1}f_{\mathrm{A}} \ \cdot {}^{0}f_{\mathrm{A}} \big/ \left({}^{0}f_{\mathrm{A}} + \ f_{\mathrm{A}}\right)$

else

$\alpha_1 = \alpha_0$

$^{1}f_{\mathrm{A}} = {}^{0}f_{\mathrm{A}}$

endif

$\alpha_0 = \alpha$

$^{0}f_{\mathrm{A}} = f_{\mathrm{A}}$

endo

2 *continue*

STOP !Algorithm stops (too many iterations)

3 *continue*

endif

Figure C.1 Typical intersection problem using Pegasus algorithm (Dowell and Jarratt, 1972)

9. REFERENCES

1. Abbo AJ. Finite element algorithms for elastoplasticity and consolidation. PhD thesis, University of Newcastle, Australia, (1997).
2. Alonso EE, Gens A, Josa A. A constitutive model for partially saturated soils. Géotechnique, 40(3) (1990), pp. 405–430.
3. Borja RI, White JA. Continuum deformation and stability analyses of a steep hillside slope under rainfall infiltration. Acta Geotech, 5 (2010), pp. 1–14.
4. Cattaneo F, Vecchia GDella, Jommi C. Evaluation of numerical stress-point algorithms on elastic–plastic models for unsaturated soils with hardening dependent on the degree of saturation. Computers and Geotechnics, 55 (2014), pp. 404–415.
5. Dormand JR, Prince PJ. A family of embedded Runge-Kutta formulae. Journal of Computational and Applied Mathematics, 6(1) 1980, pp. 19–26.
6. Dowell M, Jarratt P. The Pegasus method for computing the root of an equation, BIT, 12 (1972), pp. 503–8.
7. Gallipoli D, Gens A, Sharma R, Vaunat J. An elasto-plastic model for unsaturated soil incorporating the effects of suction and degree of saturation on mechanical behaviour. Géotechnique, 53(1) (2003), pp. 123–136.
8. Gens A. Soil–environment interactions in geotechnical engineering. Géotechnique, 60(1) (2010), pp. 3–74.
9. Houlsby GT. The work input to an unsaturated granular material. Géotechnique, 47(1) (1997), pp. 193–196.
10. Jommi C, Di Prisco C. A simple theoretical approach for modelling the mechanical behaviour of unsaturated granular soils (in Italian) Il ruolo dei fluidi in ingegneia geotecnica. Proc. of Italian conf. Mondovi, (1994), pp. 167–188.
11. Khalili N., Habte M.A., & Zargarbashi S. A fully coupled flow deformation model for cyclic analysis of unsaturated soils including hydraulic and mechanical hysteresis Comp. Geotech., 35(6) (2008), pp. 872–889.
12. Lloret-Cabot M, Sánchez M, Wheeler SJ. Formulation of a three-dimensional constitutive model for unsaturated soils incorporating mechanical-water retention couplings. International Journal for Numerical and Analytical Methods in Geomechanics, 37 (2013), pp. 3008–3035.
13. Lloret-Cabot M, Sloan SW, Sheng D, Abbo AJ. Error behaviour in explicit integration algorithms with automatic substepping. International Journal for Numerical Methods in Engineering, 108(9) (2016), pp. 1030–1053.

14. Lloret-Cabot M, Wheeler SJ, Pineda JA, Romero E, Sheng D. From saturated to unsaturated conditions and vice versa. Acta Geotech., 13(1) (2018a), pp. 15–37.
15. Lloret-Cabot M, Wheeler SJ, Pineda JA, Romero E, Sheng D. Reply to Discussion of “From saturated to unsaturated conditions and vice versa”. Acta Geotech., 13(2) (2018b), pp. 493–495.
16. Lloret-Cabot M, Wheeler SJ, Sánchez M. A unified mechanical and retention model for saturated and unsaturated soil behaviour. Acta Geotech., 12(1) (2017), pp. 1–21.
17. Lloret-Cabot M, Wheeler SJ, Sánchez M. Unification of plastic compression in a coupled mechanical and water retention model for unsaturated soils. Can. Geotech. J., 51(12) (2014), pp. 1488–1493.
18. Lloret-Cabot M, Wheeler, SJ. The mechanical yield stress in unsaturated and saturated soils. Proc. 7th Int. conf. unsat. soils (eds W.W. Ng, A.K. Leung, A.C.F. Chiu, C. Zhou), Hong Kong, HKUST, (2018), pp. 221-226.
19. Ng CWW, Pang, YW. Influence of stress state on soil-water characteristics and slope stability. J. Geotech. Eng. ASCE, 126(2) (2000), pp. 157–166.
20. Nuth M. Laloui L. Advances in modelling hysteretic water retention curve in deformable soils. Comp. Geotech., 35(6) (2008), 835–844.
21. Olivella S, Gens A, Carrera J, Alonso EE. Numerical formulation for a simulator (CODE_BRIGHT) for the coupled analysis of saline media. Engineering Computations, 13(7): (1996), pp. 87–112.
22. Pedroso DM, Sheng D, Sloan, SW. Stress update algorithm for elastoplastic models with nonconvex yield surfaces. International Journal for Numerical Methods in Engineering, 76 (2008), pp. 2029–2062.
23. Pérez-Foguet A, Rodríguez-Ferran A, Huerta A. Consistent tangent matrices for substepping schemes, Computer Methods in Applied Mechanics and Engineering, 190(35-36) (2001), pp. 4627–4647.
24. Pinyol NM, Alonso EE, Olivella, S. Rapid drawdown in slopes and embankments. Water Resources Research, 44(5) 2008, pp. 1–22.
25. Potts DM, Gens A. A critical assessment of methods of correcting for drift from the yield surface in elastoplastic finite element analysis. International Journal for Numerical and Analytical Methods in Geomechanics, 9 (1985), pp. 149–59.

26. Potts DM, Gens A. The effect of the plastic potential in boundary value problems involving plane strain deformation. International Journal for Numerical and Analytical Methods in Geomechanics, 8(3) (1984), 259–286.
27. Potts DM, Zdravkovic L. Finite element analysis in geotechnical engineering: theory, (1999). Thomas Telford, London.
28. Romero E, Gens A, Lloret A. Water permeability, water retention and microstructure of unsaturated compacted Boom clay. Eng. Geol., 54 (1999), pp. 117–127.
29. Roscoe KH, Burland JB. On the generalised stress-strain behavior of wet clay. Engineering Plasticity (eds Heyman J & Leckie FA), Cambridge University Press, Cambridge, (1968), pp. 535–609.
30. Sánchez M, Gens A, Guimarães L, Olivella S. Implementation algorithm of a generalised plasticity model for swelling clays. Computers Geotechnics, 35(6) (2008), pp. 860–871.
31. Shampine LF. Numerical Solution of Ordinary Differential Equations. Chapman & Hall, London, (1994).
32. Sheng D, Sloan SW, Gens A, Smith DW. Finite element formulation and algorithms for unsaturated soils. Part I: Theory. International Journal for Numerical and Analytical Methods in Geomechanics, 27 (2003a), pp. 745–765.
33. Sheng D, Sloan SW, Gens A, Smith DW. Finite element formulation and algorithms for unsaturated soils. Part II: Verification and Application. International Journal for Numerical and Analytical Methods in Geomechanics, 27 (2003b), pp. 767–790.
34. Sheng D, Sloan SW, Yu HS. Aspects of finite element implementation of critical state models. Computational mechanics, 26 (2002), pp. 185–196.
35. Sloan SW, Abbo AJ, Sheng D. Refined explicit integration of elastoplastic models with automatic error control. Engineering Computations, 18(1-2) (2001), pp. 121-154. Erratum: Engineering Computations, 19(5-6) (2002), pp. 594–594.
36. Sloan SW. Substepping schemes for the numerical integration of elastoplastic stress-strain relations. International Journal for Numerical Methods in Engineering, 24 (1987), pp. 893–911.
37. Sołowski WT, Gallipoli D. Explicit stress integration with error control for the Barcelona Basic Model. Part I: Algorithms formulations. Computers and Geotechnics, 37(1-2) (2010a), pp. 59–67.

38. Sołowski WT, Gallipoli D. Explicit stress integration with error control for the Barcelona Basic Model. Part II: Algorithms efficiency and accuracy. Computers and Geotechnics, 37(1-2) (2010b), pp. 68–81.
39. Sołowski WT, Sloan SW. Elastic or Elasto-Plastic: Examination of Certain Strain Increments in the Barcelona Basic Model. Proc. 2nd Eur. conf. unsat. soils (eds C Mancuso, C Jommi, F D'Onza), Naples, (2012), Springer, pp. 85-91.
40.Sołowski WT, Hofmann M, Hofstetter G, Sheng D, Sloan S. A comparative study of stress integration methods for the Barcelona Basic Model. Computers and Geotechnics, 44 (2012), pp. 22–33
41.Tarantino A. A water retention model for deformable soils. Géotechnique, 59(9) (2009), pp. 751–762.
42.Tsiampousi A, Zdravkovic L, Potts DM. Variation with time of the factor of safety of slopes excavated in unsaturated soils Computers and Geotechnics, 48(2) (2013), pp. 167–178.
43.Wheeler SJ, Sharma RS, Buisson MSR. Coupling of hydraulic hysteresis and stress–strain behaviour in unsaturated soils. Géotechnique, 53(1) (2003), pp. 41–54.
44. Zhao J, Sheng D, Rouainia M, Sloan SW. Explicit stress integration of complex soil models. International Journal for Numerical and Analytical Methods in Geomechanics, 29 (2005), pp. 1209–1229.
45.45. Zhang Y, Zhou AN. Explicit integration of a porosity-dependent hydro-mechanical model for unsaturated soils. Int J Numer Anal Meth Geomech, 40 (2016), pp. 2353-2382.
46. Zhou AN, Sheng D. An advanced hydro-mechanical constitutive model for unsaturated soils with different initial densities. Computers and Geotechnics, 63 (2015), pp. 44–66.